CALCIUM NANOPARTICLES TO STIMULATE DENDRITIC CELLS AND BOOST CELLULAR IMMUNITY OF T CELLS AGAINST CANCER

by

ZHENGWEI CAO

(Under the Direction of Jin Xie)

ABSTRACT

Dendritic cells (DCs) are the most effective type of antigen-presenting cells (APCs). DCs capture tumor antigens, process them, and migrate to the T cell zone in tumor-draining lymph nodes (TDLNs) where they prime naïve T cells through cross-presentation. During this process, DCs manifest upregulated antigen-presenting molecules (major histocompatibility complexes class I and class II - MHC-I and MHC-II) and co-stimulatory molecules (CD80, CD86 and CD40), and elevated secretion of cytokines such as interleukin 12 (IL-12) and tumor necrosis factor-α (TNF-α). After cross-presentation, naïve T cells proliferate and differentiate into effective $CD8^+$ cytotoxic T lymphocytes (CTLs) and $CD4^+$ helper T lymphocytes (T_H cells). These effective T cells travel back to tumors where $CD8^+$ CTLs kill cancer cells in an antigen-specific manner and $CD4^+$ T_H cells secrete cytokines to attract other immune cells to the site. However, tumor microenvironment (TME) is rich in immunosuppressive factors, which may suppress DC maturation and migration thus curbing T cell immunity. Many have explored immune modulators that can stimulate DCs to boost immune responses. Despite the progress, however, selectively and safely activating DCs *in vivo* remain elusive. DC responses are largely governed by Ca^{2+} signaling. During maturation, intracellular calcium of DCs is elevated, triggering signaling cascades that

result in upregulation of co-stimulatory and antigen-presenting molecules. Herein, we investigate calcium nanoparticles as a novel type of immune modulator for DCs. We postulate that these calcium nanoparticles taken up by DCs can slowly release calcium therein, thus promoting DC maturation, migration, activation and cross-presentation, in turn augmenting cellular immunity of T cells against cancer.

INDEX WORDS: cancer, cellular immunity, dendritic cell, T cell, calcium, nanoparticle, immunotherapy, radiotherapy, chemotherapy

CALCIUM NANOPARTICLES TO STIMULATE DENDRITIC CELLS AND BOOST CELLULAR IMMUNITY OF T CELLS AGAINST CANCER

by

ZHENGWEI CAO

BS, University of Science and Technology of China, China, 2013

A Dissertation Submitted to the Graduate Faculty of The University of Georgia in Partial Fulfillment of the Requirements for the Degree

DOCTOR OF PHILOSOPHY

ATHENS, GEORGIA

2022

CALCIUM NANOPARTICLES TO STIMULATE DENDRITIC CELLS AND BOOST CELLULAR IMMUNITY OF T CELLS AGAINST CANCER

by

ZHENGWEI CAO

Major Professor:	Jin Xie
Committee:	Amanda Frossard
	Leidong Mao

Electronic Version Approved:

Ron Walcott
Vice Provost for Graduate Education and Dean of the Graduate School
The University of Georgia
May 2022

DEDICATION

To families and friends who keep me protection and company, and to people who look down upon me which provides the motivation to fight.

ACKNOWLEDGEMENTS

At the end of the Ph.D. journey, I want to thank my parents who give birth to me, look after me and protect me from the world before I can protect myself and my family. There is no chance that I can survive to the end of this experience without their encouragement, support and unconditional love. I also want to thank my grandma who always cares for me and stands by my side, especially after making it through of grandpa's sudden death whom we all cared so much. Besides, I want to thank my uncle who teaches me the way how this world works, my untie who influences me to be optimistic all the time, and their son, my little brother who always sees me as idol and makes me laugh when I am down. Apart from my family, I want to thank my friends who keep me company to make it through this journey.

For my Ph.D. degree, I also would like to thank my advisor Dr. Jin Xie for his guidance through the whole program, my colleagues for their help and work in different projects. I also even want to thank those who once looked down upon and hurt me for whichever reason, who gave me the motivation to fight and became stronger to deal with whatever comes from this world.

TABLE OF CONTENTS

Page

LIST OF FIGURES

Page

CHAPTER 1

INTRODUCTION: DENDRITIC CELL, T CELL AND CANCER

Background of cancer

Cancer is one of humanity's greatest health threats which kills millions of people every year.[1] The lethality of cancer comes from the uncontrolled proliferation of abnormal cells with the capability of spreading to healthy tissues and organs.[2] Normal cells can go through abnormal changes called hyperplasia where there is an increase in the number of cells in tissue or organ that appear normal, to the stage dysplasia where cells look abnormal under a microscope but are not cancer, and finally get to the stage of cancer.[3] Cancer is a genetic disease which means it is caused by changes to genes that control the way how cells function. These genetic changes can happen due to the errors that occur as cells divide, damages to DNA caused by harmful substances in the environment and they can be inherited from parents.[4] Some risk factors for cancer include aging, alcohol, cancer-causing substances such as many types of chemicals, chronic inflammation, diet, hormones, immunosuppression, infectious agents such as bacteria and viruses, obesity, radiation such as X-ray and gamma ray, sunlight of ultraviolet exposure and tobacco.[5] All these listed factors can potentially cause cancer when the body is experiencing aberrances caused by them. There are many types of cancer treatment including surgery, chemotherapy, hormone therapy, photodynamic therapy, hyperthermia, radiation therapy and immunotherapy.[6] However, advanced cancer remains immensely difficult to treat, thus novel therapeutic approaches are desperately needed. In despite of remarkable progresses, attempts to explore new strategies against cancer proved difficult. It is

with no doubt that tremendous amount of work is needed to reveal the mysterious vails of cancer immunology, while at the same time enormous opportunities for cancer therapeutics have lied still in these mysteries waiting to be discovered.

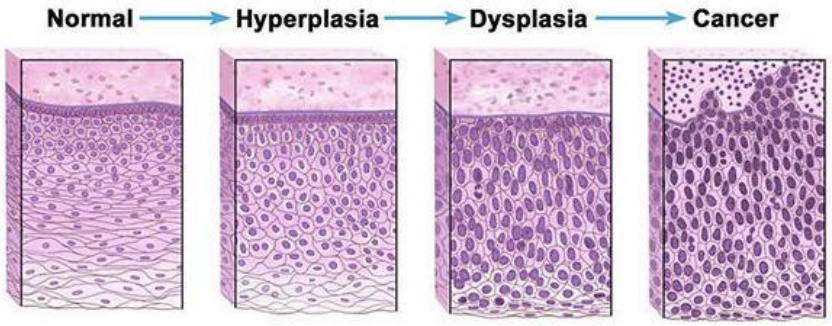

Figure 1.1. Development of different stages in cancer.

Tumor immune microenvironment

In the tumor-specific adaptive immunity, tumor-antigen capture and presentation by DCs is pivotal for initiating optimal T cell immunity against cancer.[7] However, in the complicated tumor microenvironment, cancer cells are in return capable of developing various strategies to compromise the immunosurveillance of anticancer immune responses.[8] Immunosuppressive factors from cancer cells can suppress DC infiltration and survival and impair cross-presentation, curbing immunity or inducing tolerance.[9] The myeloid-derived suppressor cells (MDSCs)[10] and tumor-associated macrophages (TAMs)[11] along with expression of immunosuppressive cytokines such as interleukin-10 (IL-10)[12] and transforming growth factor-β (TGF-β)[13] adversely affect DC function in tumor, resulting in the DC phenotypes usually carrying an "immature" phenotype. IL-10 is an anti-inflammatory cytokine which can downregulate the expression of T_H 1 cytokines, MHC class II and co-stimulatory molecules on DCs.[12] TGF-β is also a cytokine which can

suppressive anticancer immunity. It can precipitate the expression of FOXP3 and convert differentiation of effector T helper cells to immunosuppressive $CD4^+$ regulatory T (Treg) cells, as well as causing angiogenesis and immunosuppression which makes the cancer more invasive.[13] The accumulation of immature DCs also promote the expansion of immunosuppressive $CD4^+$ regulatory T (Treg) cells associated with further immunosuppressive cytokine secretion (e.g. IL-10, TGF-β) and tumor progression.[14] Therefore, accelerating DC function in tumor at an early stage is essential for eliciting T cell immune response against cancer.

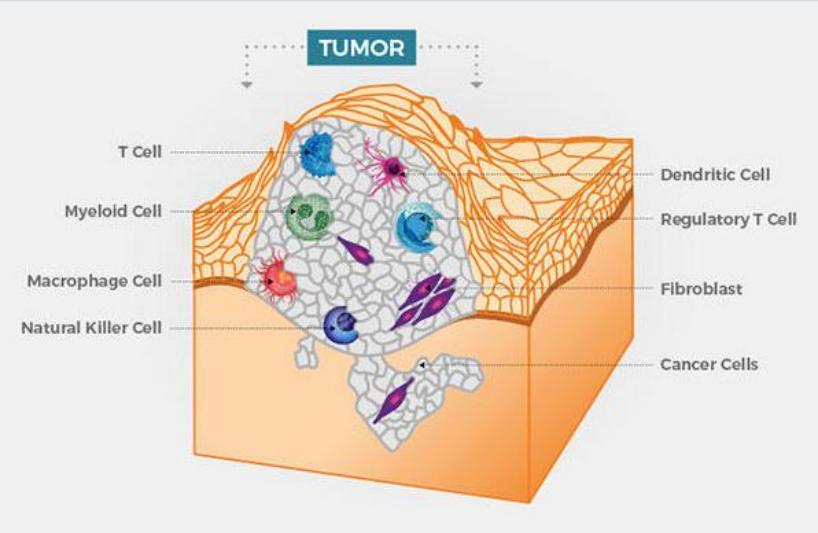

Figure 1.2. Tumor microenvironment.

T cell immunity in cancer

In the complex tumor microenvironment, there are not only cancer related cells but also many types of immune cells.[15] Immune system is highly effective in detecting and eliminating foreign infectious agents and abnormal cells in the tissues, but cancer cells are native to the body and in many respects indistinguishable from the normal cells.[16] Humoral immune response generates soluble antibody molecules capable of specifically recognizing and binding antigens,

which results in the neutralization of antigens or coating infected cells with antibodies, leading to recognition, engulfment and destroy of these infections by phagocytic macrophages or killing by cytotoxic natural killer (NK) cells.[17] However, this arm of immune defense fails its efficiency with antigens inside cells shielded by plasma membrane as in the case of cancer, where the aberrant proteins are hiding deep within the cells. One group of immune cells that can efficiently fight cancer is T cell. One essential type of effective T cells is $CD8^+$ cytotoxic T lymphocytes (CTLs), which can recognize tumor antigens on tumor cells and kill tumor cells. Another essential cell type is $CD4^+$ helper T lymphocytes (T_H cells), which can secrete cytokines to activate other immune cells such as NK cells and macrophages, induce inflammation as well as proliferation and differentiation of both effective $CD8^+$ and $CD4^+$ T cells.[18] Before turning effective, these T cells are just naïve T cells resting at lymphoid organs such as spleen and lymph node. Naïve T cells get activated after antigen recognition from antigen-presenting cells (APCs), then proliferate and differentiate into effective $CD8^+$ and $CD4^+$ T cells, called T cell priming.[19] After priming, these effective T cells will obtain tumor-specific adaptive immunity where $CD4^+$ T_H cells secrete cytokines and $CD8^+$ CTLs recognize and kill tumor cells.[20] To get tumor-specific adaptive immunity, T cells must be presented of tumor antigens in advance and this duty is designated to APCs.

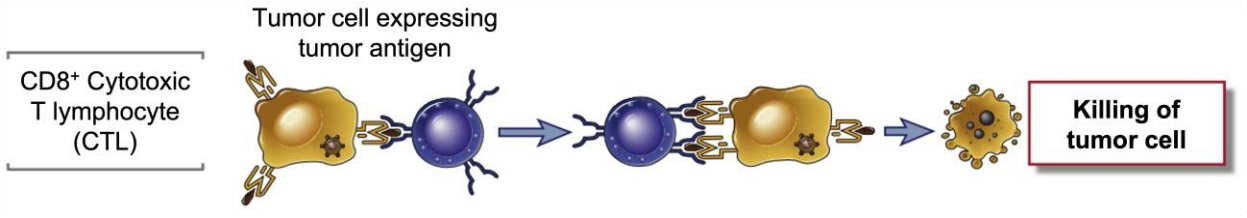

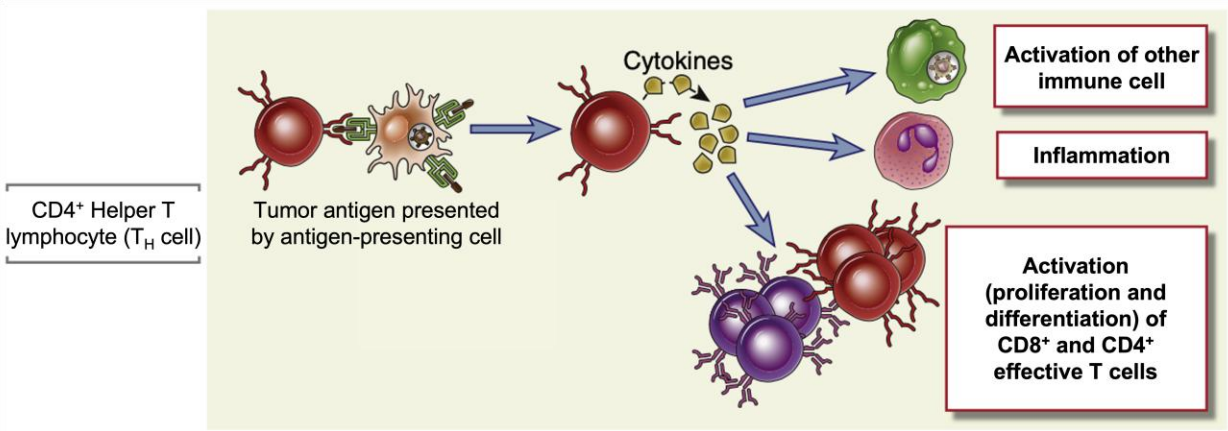

Figure 1.3. Effective $CD8^+$ and $CD4^+$ T cells in anticancer immunity.

Dendritic cell in T cell immunity

As the most effective type of antigen-presenting cells (APCs), DCs are specialized with the task of internalizing antigens and presenting ingested antigens to various types of T cells.[21] They capture tumor antigens, process them into peptides to bind antigen-presenting molecules, and migrate to the T cell zone in tumor-draining lymph nodes (TDLNs) where they prime naïve T cells through cross-presentation.[22] During this process, DCs manifest upregulated antigen-presenting molecules (major histocompatibility complexes class I and class II - MHC-I and MHC-II) and co-stimulatory molecules (CD80, CD86 and CD40), and elevated secretion of cytokines such as interleukin 12 (IL-12) and tumor necrosis factor-α (TNF-α). DCs use MHC class II to present antigens to T cell receptor (TCR) on $CD4^+$ T cells,[23] and MHC class I to $CD8^+$ T cells respectively which is called antigen cross-presentation.[24] They also express co-stimulators such as CD80, CD86 to bind CD28 on T cell to stimulate T cell activation,[25] and CD40 to bind CD40L on T cell to enhance DC activation, CD80/CD86 expression and cytokine secretion.[26] Besides, DCs secrete cytokines such as interleukin-12 (IL-12) to activate T cells' proliferation and differentiation,[27] as well as interferon-γ (IFN-γ) production which in return can activate DCs.[28] In

one word, DCs and T cells form a positive loop in this process to activate T cell immunity. After cross-presentation, naïve T cells are able to activate their programed functions that they proliferate and differentiate into effective $CD8^+$ CTLs and $CD4^+$ T_H cells which then travel back to tumors where $CD8^+$ CTLs kill cancer cells in an antigen-specific manner and $CD4^+$ T_H cells secrete cytokines to attract other types of immune cells.[29]

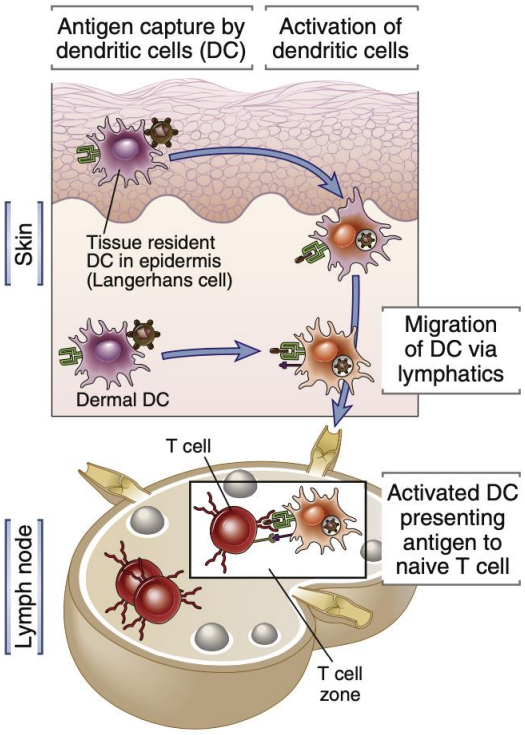

Figure 1.4. Dendritic cells in T cell immunity.

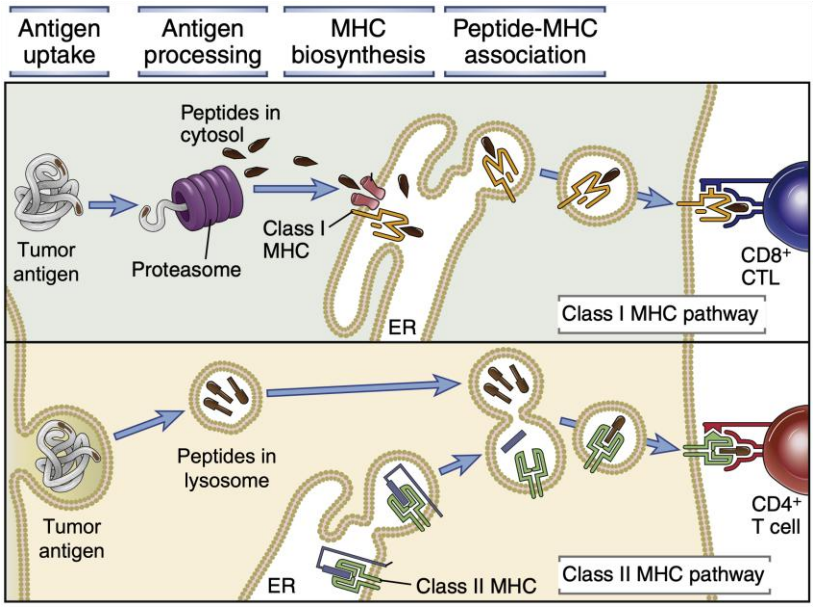

Figure 1.5. Dendritic cells process and present tumor antigens to T cells.

Role of Ca^{2+} in dendritic cell

DC responses are largely governed by Ca^{2+} signaling.[30] While resting immature DCs maintain a low-level cytosolic calcium, intracellular calcium or $[Ca^{2+}]_{int}$ is drastically increased during DC maturation, initiating signaling cascades that cause upregulation of co-stimulatory and antigen-presenting molecules.[31] DC $[Ca^{2+}]_{int}$ is tightly regulated by calcium-selective ion channels and transporters present on the plasma membrane, endoplasmic reticulum, and inner mitochondrial membrane.[32] Previously, calcium ionophores (e.g. ionomycin) are used to induce elevation of $[Ca^{2+}]_{int}$ and activate DCs *in vitro*.[33] However, these conventional ionophores lack DC specificity, and may be toxic to normal tissues. Moreover, DC maturation and activation demands an endured increase of $[Ca^{2+}]_{int}$ rather than a spike. That is, the extracellular level of ionophore needs to be maintained at a high level for sustained $[Ca^{2+}]_{int}$ elevation, which is challenging *in vivo* due to their rapid clearance of small molecule ionophores.[34] There is an unmet goal of developing safe calcium modulators that can selectively stimulate DCs to boost DC-mediated anticancer immunity.

Herein, we investigate $Ca(OH)_2$ nanoparticles (CHNPs) as a novel type of immunomodulator for DC activation. We postulate that calcium nanoparticles when taken uptake by DCs can slowly release calcium therein; this results in an increase of $[Ca^{2+}]_{int}$ that promotes DC maturation, migration, and cross-presentation, in turn augmenting cellular immunity of T cells. For surface modification, we coated $Ca(OH)_2$ nanoparticles with silica and PEGylated the surface, and then coupled to the particles anti-CD205 antibodies. CD205 or DEC205 is a type I integral membrane protein expressed primarily on DCs and investigated pre-clinically and clinically for targeted delivery of antigens to DCs.[35] We envision that the resulting AnCHNPs can synergize with existing treatment options to elicit a robust anti-cancer immunity. For proof-of-concept, we tested combination therapy with AnCHNPs and other therapies such as radiotherapy (RT), chemotherapy and immunotherapy. RT causes immunogenic cell death (ICD) of cancer cells, releasing tumor antigens and damage-associated molecular patterns (DAMPs) into the TME. However, RT alone is often insufficient to elicit a robust immunity. We postulate that AnCHNPs can serve as an adjuvant for DCs to boost RT-induced T cell immunity in particular to augment tumor suppression. We tested the hypothesis first *in vitro* with bone marrow derived dendritic cells (BMDCs) and then *in vivo* in multiple transplanted models.

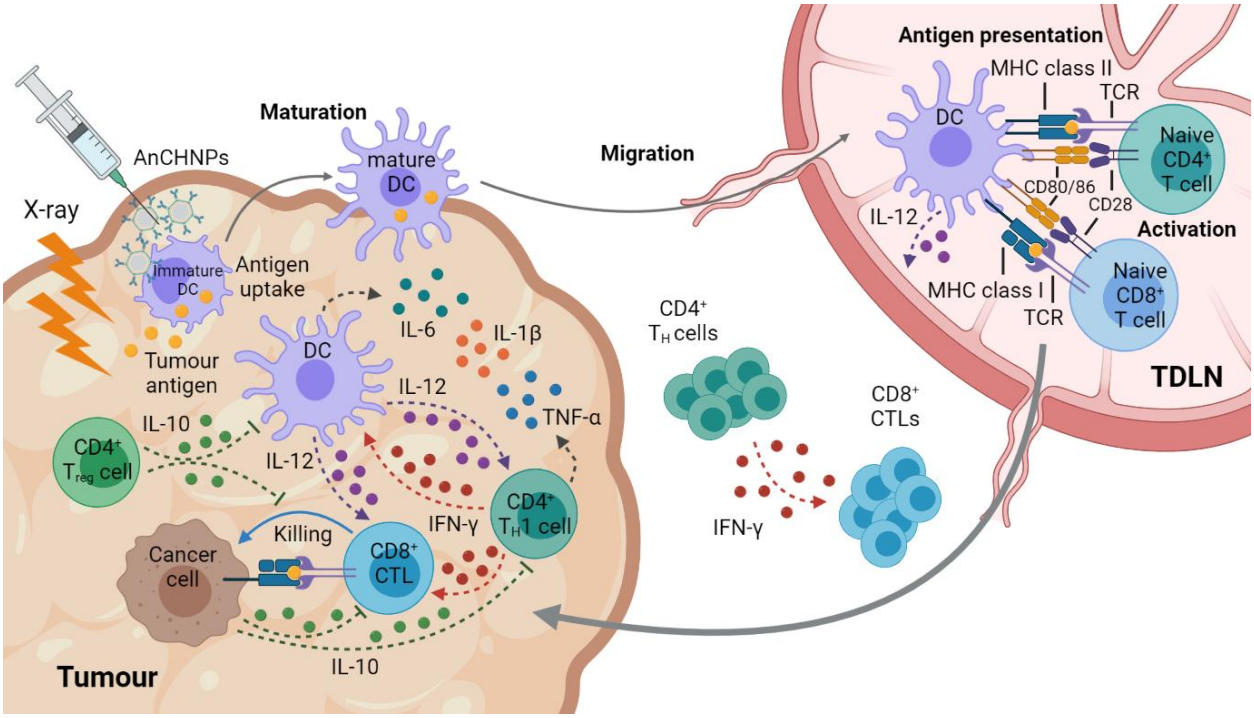

Figure 1.6. Proposed mechanism of DC stimulation and T cell immunity boost by AnCHNPs.

CHAPTER 2

SYNTHESIS AND CHARACTERIZATIONS OF CALCIUM HYDROXIDE NANOPARTICLES

Synthesis of $Ca(OH)_2$ nanoparticles

Synthesis of calcium hydroxide/$Ca(OH)_2$ nanoparticles (CHNPs)

We synthesized CHNPs using a co-precipitation method in water (**Figure 2.1 a**). Typically, 443.92 mg of calcium chloride ($CaCl_2$, anhydrous, 97%, Sigma-Aldrich, Lot # SLBQ3073V) was dissolved in 18.571 mL Milli Q H_2O, then 1.429 mL of 6 M sodium hydroxide (NaOH, Fisher, Lot # 166374) solution was added dropwise into previous solution and the mixture solution was kept magnetically stirred for 5 mins at 90 °C. The raw products were collected by centrifugation at 8000 RPM for 5 mins. Then the particles were redispersed in ethanol (200 proof, Koptec, Lot # 274014) with brief sonication and centrifugation/ethanol washing process was repeated 3 times to remove unreacted precursors.

Silica-coated calcium hydroxide/$Ca(OH)_2$ nanoparticles (SCHNPs)

We then coated CHNPs with silica using TEOS and APTES as silane precursors and subsequently PEGylate the particle surface with PEG diacid (m.w.=2000). The above-synthesized CHNPs of 50 mg were dispersed in a mixture solution of 40 mL ethanol and 0.4 mL ammonia (28.0-30.0%, J.T.Baker, Lot # 0000010971). The solution was then set under vigorous stirring for 30 mins following sonication of 30 s. Afterwards, 300 μL of TEOS (Tetraethyl orthosilicate, 98%,

Sigma-Aldrich, Lot # STBJ8253) was added into the solution dropwise, followed by 180 µL of APTS ((3-Aminopropyl)triethoxysilane, 98%, Sigma-Aldrich, Lot # MKCM7627) dropwise. Then the mixture solution was set under vigorous stirring for 20 h at room temperature. SCHNPs were collected by centrifugation at 8000 RPM for 8 mins and 3 times repeated ethanol washing process.

PEG-diacid coated calcium hydroxide/$Ca(OH)_2$ nanoparticles (PCHNPs)

Then SCHNPs of 20 mg were dispersed in 10 mL DMSO (Dimethyl sulfoxide, 99.9%, Sigma-Aldrich, Lot # MKBF8194V) in a 20 mL glass vial, kept stirring. PEG-diacid (MW 2000, JenKem tech, Lot # ZZ192P158) of 200 mg, EDC (N-(3-Dimethylaminopropyl)-N′-ethylcarbodiimide, 97%, Sigma-Aldrich, Lot # 507429) of 20 mg and NHS (N-Hydroxysuccinimide, 98%, Sigma-Aldrich, Lot # 130672) of 15 mg were dissolved in another 10 mL DMSO, which was then added into previous DMSO suspension dropwise. The mixture solution was kept stirring at 60 ℃ for 20 h. PCHNPs were collected by centrifugation at 8000 RPM for 8 mins and 2 times repeated Milli Q H_2O washing process.

Anti-CD205 coating of PEG-diacid coated calcium hydroxide/$Ca(OH)_2$ nanoparticles (AnCHNPs)

We next coupled anti-CD205 antibodies onto PCHNPs. The above-synthesized PCHNPs of 0.5 mg were dispersed in 1 mL cold sterile PBS and kept under stirring at 4 ℃. Anti-CD205 antibody (Mouse monoclonal HD30, Sigma-Aldrich, Lot # 531834) of 10 µL was added into previous PBS solution. After 25 mins of stirring, 2 µL ethanolamine (99%, Sigma-Aldrich, Lot # 398136) was added into solution for another 5 mins stirring. Afterwards, AnCHNPs were collected by centrifugation at 10000 RPM for 5 mins and PBS washing step once. Fresh-made AnCHNPs were used for *in vitro* and *in vivo* studies unless specified otherwise.

Characterizatiose of $Ca(OH)_2$ nanoparticles

Scanning electron microscopy (SEM) and transmission electron microscopy (TEM) revealed that CHNPs were hexagonal in shape (**Figure 2.1 b, c**). The average diameter (the long diagonal of the hexagon) of the nanoparticles was 219.9 ± 17.8 nm (**Figure 2.1 h**). X-ray powder diffraction (XRD) confirmed that the main component of the nanocrystal is hexagonal sheet phase $Ca(OH)_2$ (PDF # 01-073-5492, **Figure 2.1 g**).

SEM and Energy dispersive spectroscopy (EDS) confirmed the Ca core/Si shell structure of the resulting nanoparticles (**Figure 2.1 d, f; Figure S2.1 a, Appendices A**). TEM revealed that the silica coating thickness is ~30 nm (**Figure 2.1 e**). XRD suggests that silica coating did not affect the composition of the $Ca(OH)_2$ core (**Figure 2.1 g**). Nanoparticles' hydrodynamic size slightly increased from 227.3 ± 27.02 nm to 245.2 ± 30.26 nm over the PEGylation (**Figure 2.1 h**). Meanwhile, surface zeta potential changed from positive to virtually neutral (**Figure 2.1 i**). Successful PEGylation was further confirmed by Fourier-transform infrared (FT-IR). Specifically, spectra also confirmed the successful coatings of silica and PEG-diacid. The unique O-H stretching peak at 3642 cm^{-1} and C-O vibration peak of carbonate groups at 1464 cm^{-1} indicated the presence of $Ca(OH)_2$ core, the $-CH_3$ asymmetric stretching peak at 2975 cm^{-1}, $-CH_2$ asymmetric and symmetric stretching peaks at 2927 cm^{-1} and 2864 cm^{-1}, Si-O-C stretching peak at 1167 cm^{-1}, Si-O-Si stretching peak at 1080 cm^{-1} of SCHNPs proved the successful coating of silica, and the C-H stretching peak at 2882 cm^{-1}, C-H bending peaks at 1467 cm^{-1} and 1341 cm^{-1}, C-O-C stretching peak at 1033 cm^{-1} of PCHNPs proved the successful coating of PEG-diacid (**Figure S2.2 a, Appendices A**).

The resulting anti-CD205 conjugates (designated as AnCHNPs) were stable in water (**Figure 2.1 j, photo**). The antibody coupling slightly increased the hydrodynamic size of the nanoparticles (**Figure 2.1 h**) and increase the surface charge (**Figure 2.1 i**).

Conclusion

Calcium hydroxide nanoparticles of hexagonal morphology were successfully synthesized via co-precipitation method and further silica, PEG and anti-CD205 coating were successfully conjugated onto nanoparticles' surfaces which gave the final formula of nanoparticles as AnCHNPs.

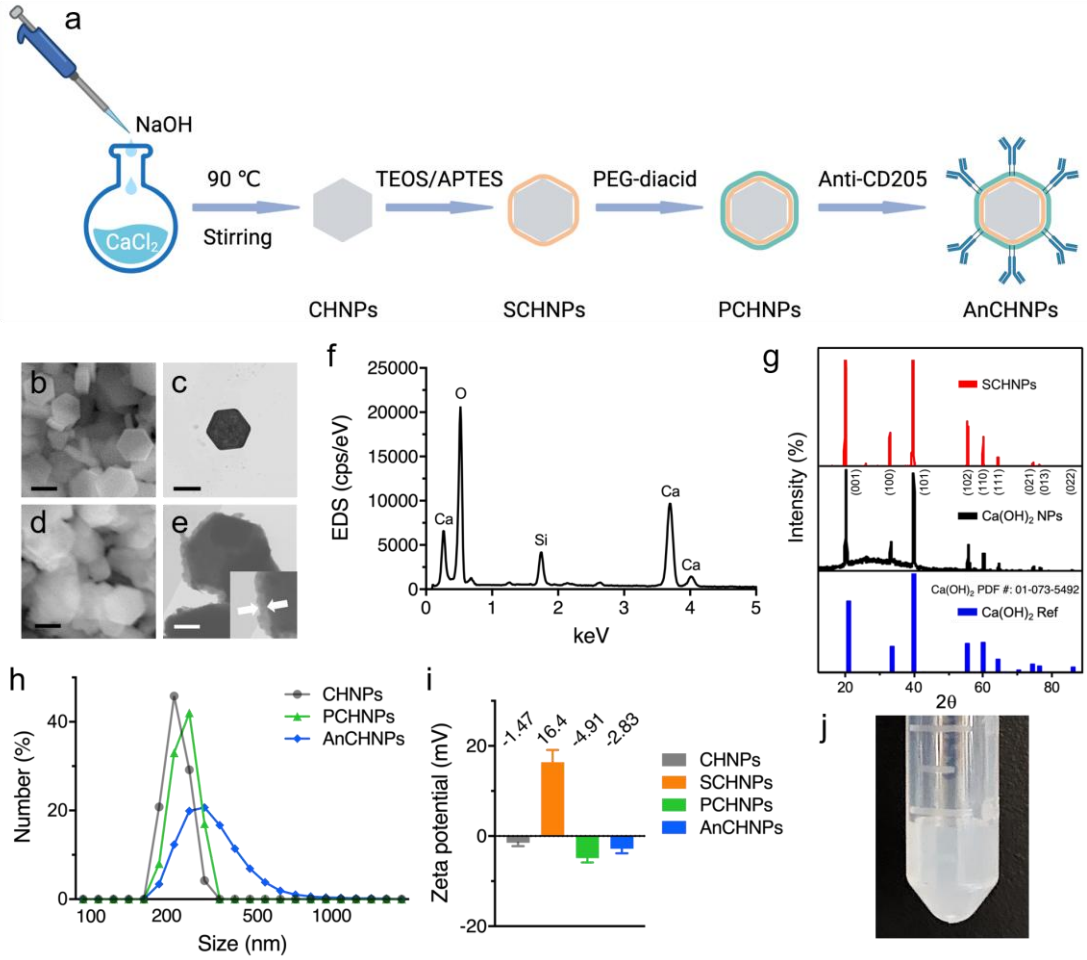

Figure 2.1. Synthesis and characterizations of $Ca(OH)_2$ nanoparticles. **a)** Synthesis flow. **b)** SEM image of CHNPs. **c)** TEM image of CHNPs. **d)** SEM image of SCHNPs. **e)** TEM image of SCHNPs. **f)** EDS spectra of SCHNPs. **g)** XRD spectra of $Ca(OH)_2$ reference, CHNPs and SCHNPs. **h)** Size distributions of CHNPs, PCHNPs and AnCHNPs. **i)** Zeta-potentials of CHNPs, SCHNPs, PCHNPs and AnCHNPs. **j)** Suspension of AnCHNPs in water. Scale bars, black 200 nm, white 100 nm.

CHAPTER 3

IN VITRO STUDY OF CALCIUM HYDROXIDE NANOPARTICLES ON DC

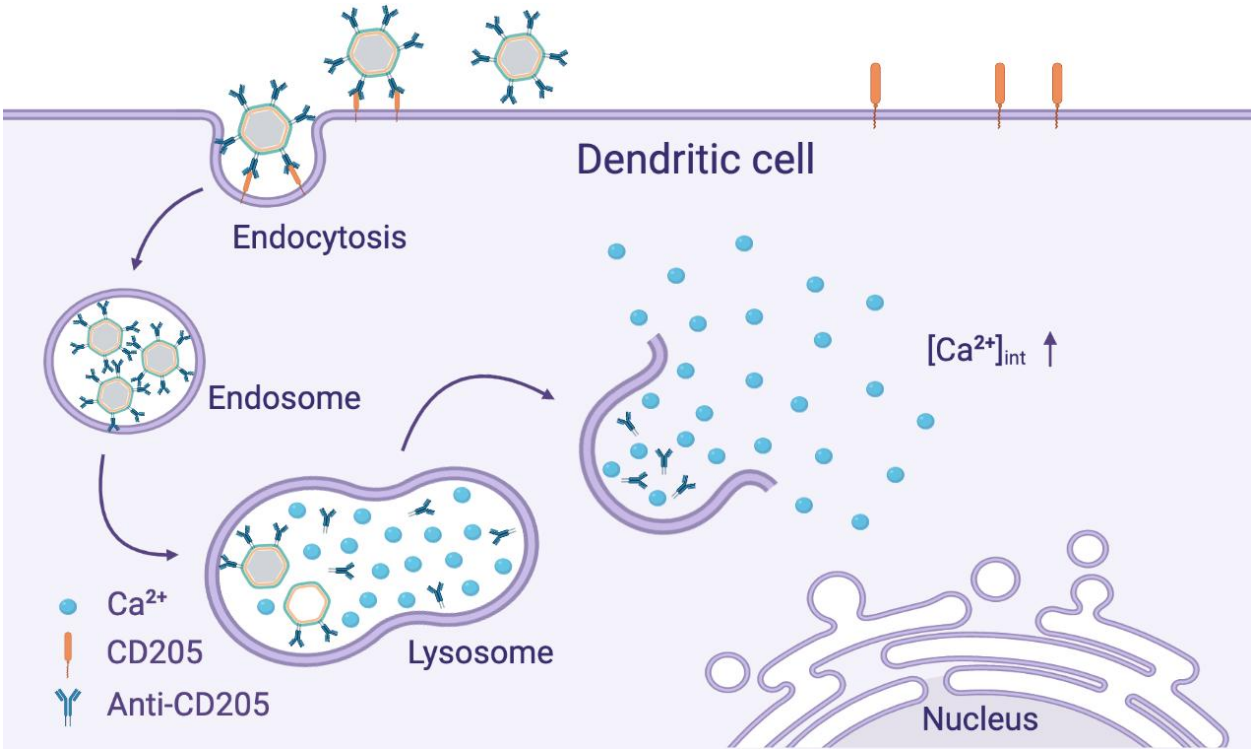

Figure 3.1. Proposed mechanism of AnCHNPs internalization and Ca^{2+} release in DC.

Stability and Ca^{2+} release in solution

We measured calcium release of CHNPs and AnCHNPs in buffer solutions (pH = 7.4 or 5.5) using a calcium-selective electrode (**Figure 3.2 b**). Calcium is slowly released from CHNPs through hydrolysis at both neutral and acidic pH. The release is moderately retarded when the nanoparticles being coated with silica. TEM images taken with samples from different time points

also revealed gradual degradation of the $Ca(OH)_2$ core, leaving a largely emptied silica shell after 12 h (**Figure 3.2 a**).

AnCHNPs uptake and Ca^{2+} release in DC

We studied the uptake of AnCHNPs by BMDCs. We labeled AnCHNPs with Cy5 and incubated them with BMDCs at 5 or 10 μg/mL (Ca concentration, same as below). For comparison, we also tested PCHNPs at the same calcium concentrations. Flow cytometry found significantly increased Cy5 uptake with AnCHNPs relative to PCHNPs (**Figure 3.2 c**), suggesting αCD205-mediated endocytosis of nanoparticles. This is consistent with others' observation that DEC205 internalizes upon antibody binding[1,2] and can thus function as an endocytic receptor[1,3]

LysoSensor™ Yellow/Blue DND-160 (PDMPO) assay found time-dependent increase of lysosomal pH (**Figure 3.2 d**), indicating that nanoparticles neutralized protons in lysosomes. Meanwhile, Fluo-3AM assay found time-dependent increase of intracellular calcium concentration ($[Ca^{2+}]_{int}$) in cells incubated with AnCHNPs (**Figure 3.2 e**). On the contrary, $CaCl_2$ salt solutions at the same calcium concentrations induced little $[Ca^{2+}]_{int}$ increase. Overall, these results confirmed that AnCHNPs were taken up by BMDCs and degraded inside cells, causing an elevation of $[Ca^{2+}]_{int}$.

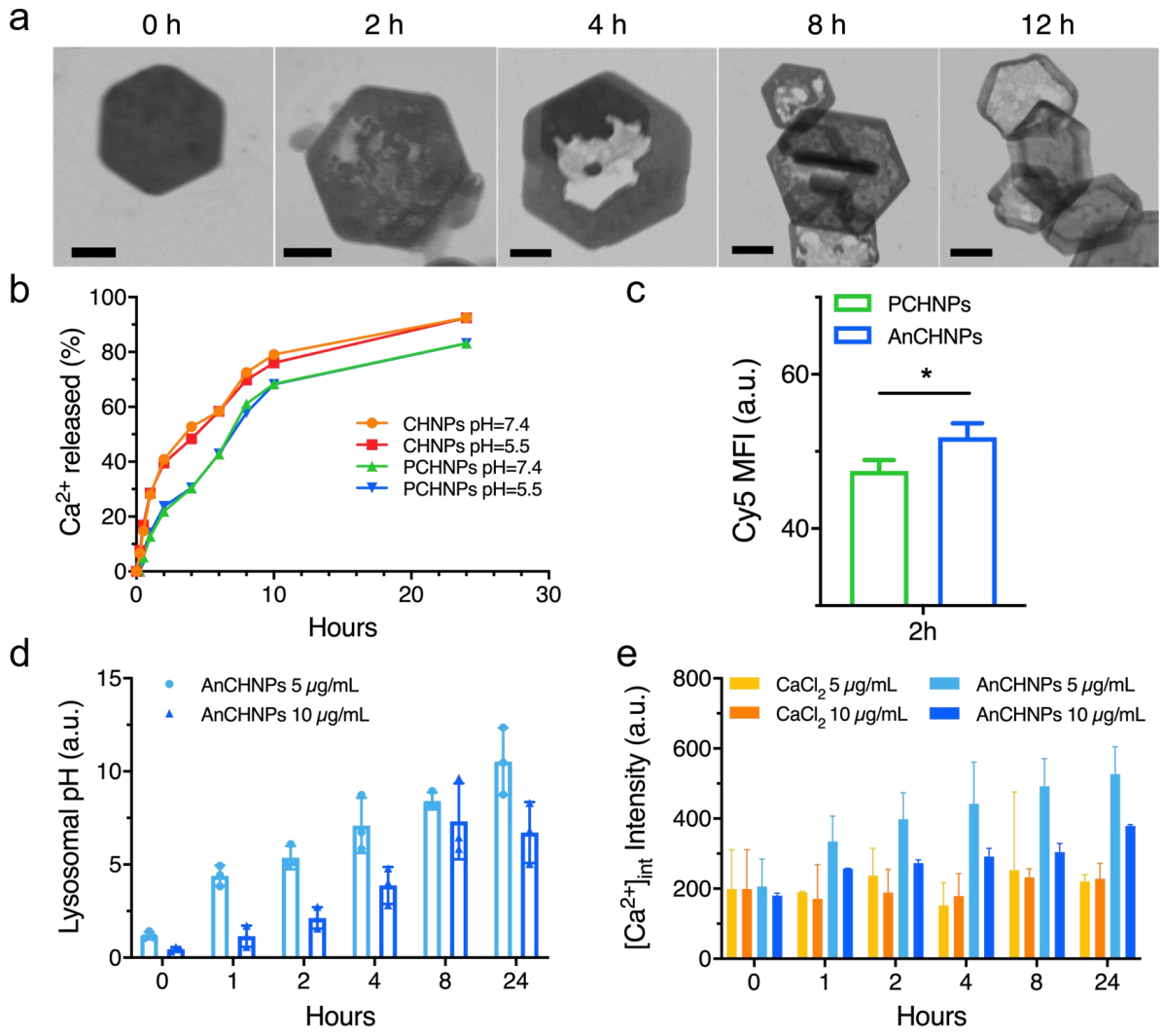

Figure 3.2. Stability and intracellular responses of AnCHNPs in DC. **a)** Degradation of PCHNPs in water by TEM. **b)** Ca^{2+} release of CHNPs and PCHNPs in ammonium acetate buffer at pH 7.4 and 5.5. **c)** Cy5 cellular uptake of PCHNPs and AnCHNPs. **d)** Lysosomal pH change of DC treated with 5 μg/mL and 10 μg/mL AnCHNPs. **e)** $[Ca^{2+}]_{int}$ change of DC treated with 5 μg/mL and 10 μg/mL AnCHNPs and $CaCl_2$ solutions. Scale bar: 100 nm.

Maturation, Migration, Activation and Antigen-presentation of DC

We next explored the impact of AnCHNPs on DCs' differentiation and functions. We incubated AnCHNPs with BMDCs at 5 or 10 μg/mL and analyzed expression of MHC-II on cell

surface. For comparison, we also tested $CaCl_2$ (5 or 10 µg/mL). Relative to untreated DCs, the MHC-II$^+$ population in CD11c$^+$ DCs increased by 85% or 35% after cells being treated with 5 µg/mL or 10 µg/mL AnCHNPs (**Figure 3.3 d**), as well as increase of mean fluorescence intensity-MFI (**Figure 3c**). The CD11c$^+$MHC-II$^+$ population increased from 36% to 50% after treatment with 5 µg/mL AnCHNPs (**Figure 3.3 a**). Interestingly, treatment with AnCHNPs also induced CD205$^+$ expression on DCs (**Figure 3.3 b, e, f**), potentially creating a positive feedback loop that induces more uptake of AnCHNPs, furthering cell maturation. Note that $CaCl_2$ at the same calcium concentrations had no impact on MHC-II or CD205 regulation.

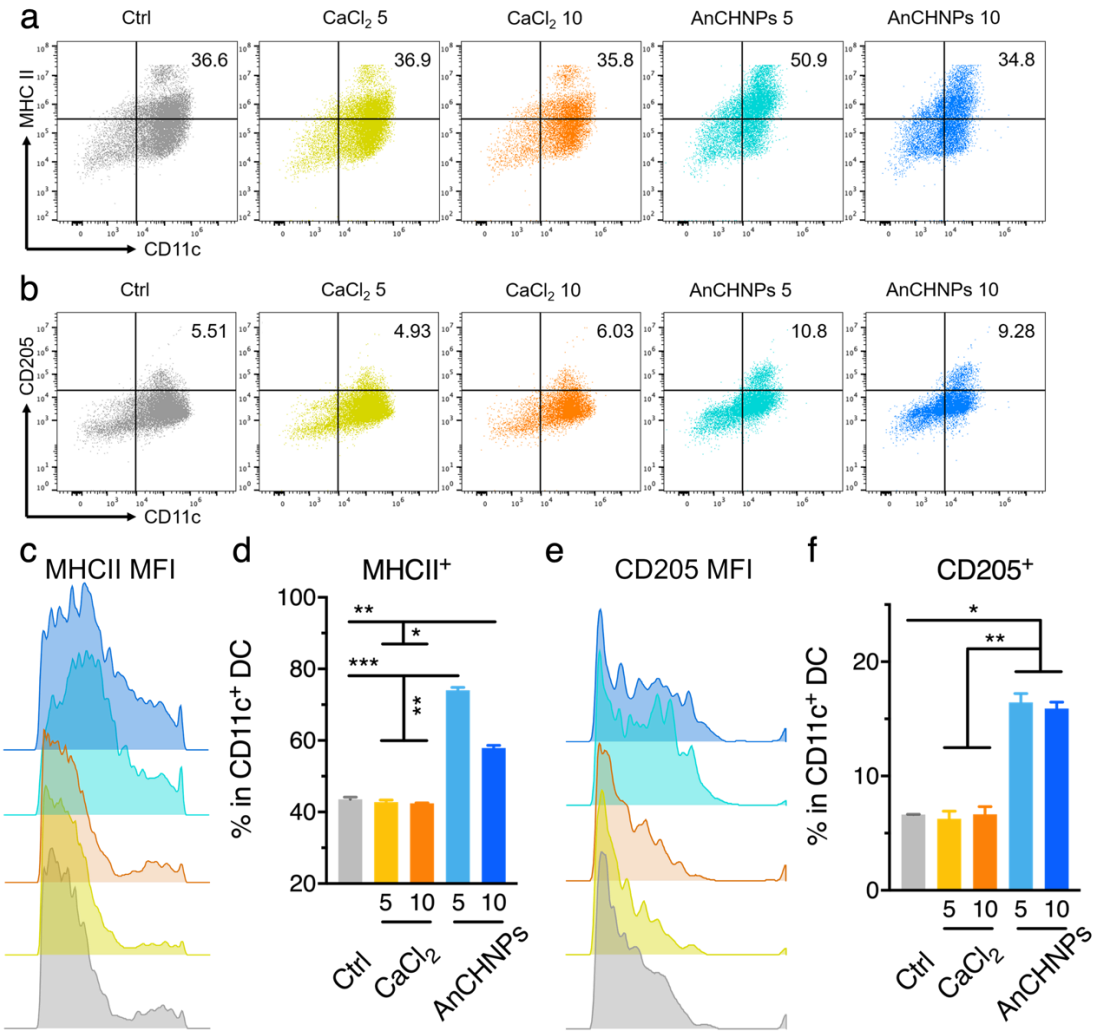

Figure 3.3. Maturation of DC. **a)** Flow cytometry gating of CD11c and MHC-II population of DC. **b)** Flow cytometry gating of CD11c and CD205 population of DC. **c)** Mean fluorescence intensity (MFI) of MHC-II. **d)** MHC-II$^+$ population in CD11c$^+$ DC. **e)** Mean fluorescence intensity (MFI) of CD205. **f)** CD205$^+$ population in CD11c$^+$ DC. Concentration unit: μg/mL.

Next, we examined DC activation and maturation when exposed to cancer cell debris. We first assessed the impact of AnCHNPs on migration of DCs in a transwell assay, where B16F10-OVA cells were seeded into the lower chamber and CFSE-labeled BMDCs loaded into the upper chamber well insert (**Figure 3.4 a**). The number of DCs migrating to the lower chamber was increased when B16F10-OVA cells were first exposed to irradiation, which is attributed to RT-induced release of alarmin signals. Applying AnCHNPs, but not $CaCl_2$, significantly promoted DC migration (**Figure 3.4 b**).

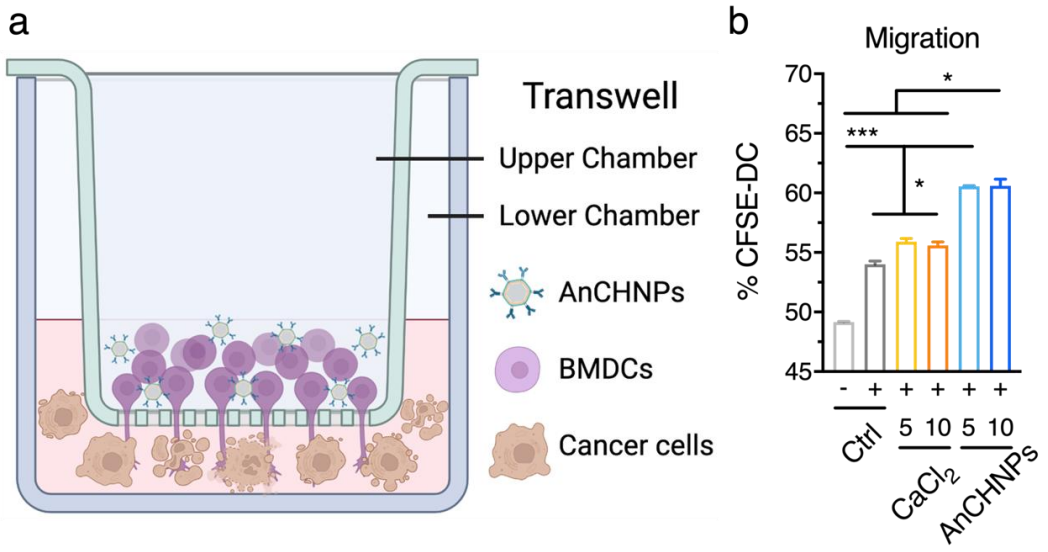

Figure 3.4. Migration of DC. **a)** Scheme of transwell assay for DC migration study. **b)** Percentage of DC migrated into lower chamber after 24 h. -: w/o X-ray irradiation; +: w/ X-ray irradiation; Concentration unit: μg/mL.

We also examined expression of maturation markers (MHC-II, CD40, CD80, and CD86) on the surface of DCs when cultured with cells debris of B16F10-OVA after RT. Adding AnCHNPs to the incubation medium significantly increased abundances of MHC-II$^+$ (**Figure 3.5 e**), CD40$^+$ (**Figure 3.5 d**), CD80$^+$ and CD86$^+$ populations (**Figure 3.5 a, c**), suggesting cell maturation. Of note, AnCHNPs in general worked more efficiently at 5 μg/mL than 10 μg/mL, which was probably attributed to the slight negative impact of AnCHNPs on cell viability at the higher concentration (**Figure S2.2 d, Appendices A**). SIINFEKL-H-2K expression also significantly elevated (**Figure 3.5 b, f**), indicating enhanced antigen presentation when DCs were treated with AnCHNPs.

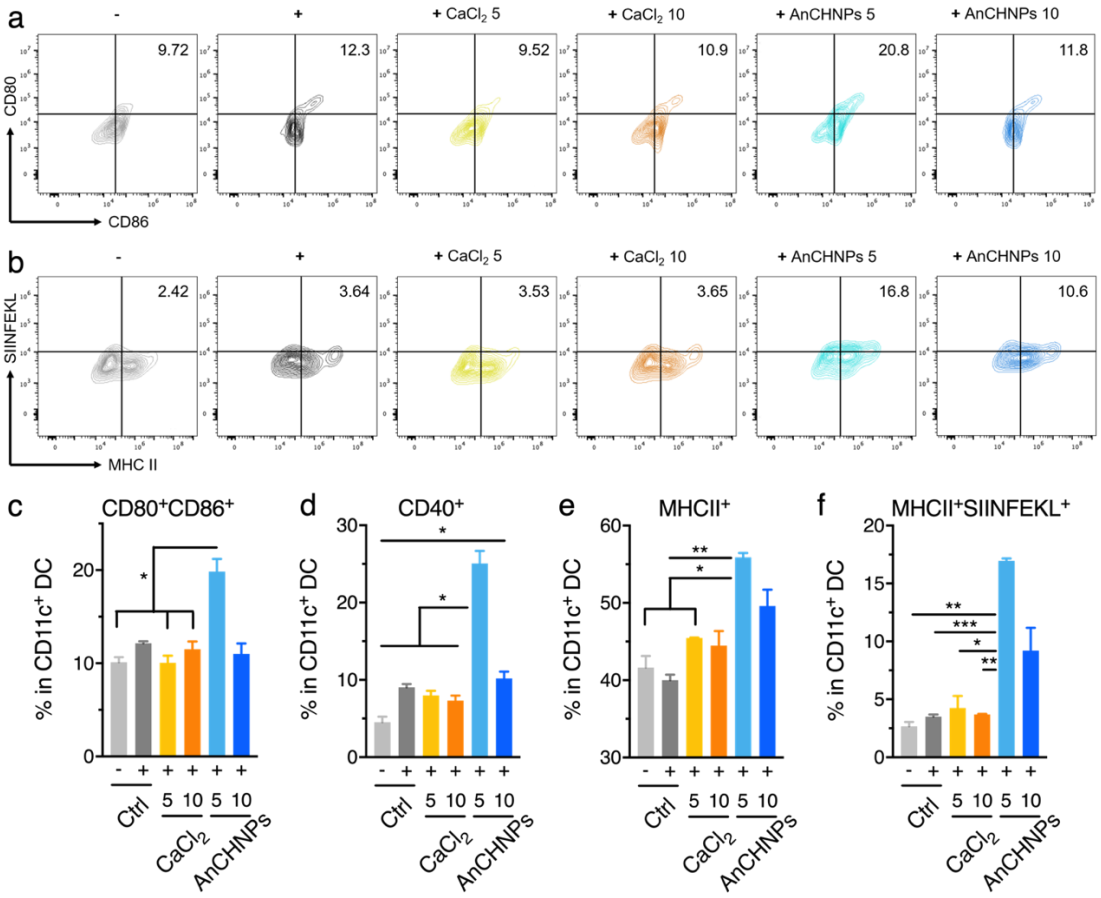

Figure 3.5. Activation and antigen-presentation of DC. **a)** Flow cytometry gating of CD80 and CD86 population of DC. **b)** Flow cytometry gating of MHC-II and SIINFEKL-H-2K population of DC. **c)** $CD80^+CD86^+$ population in $CD11c^+$ DC. **d)** $CD40^+$ population in $CD11c^+$ DC. **e)** $MHC\text{-}II^+$ population in $CD11c^+$ DC. **f)** $MHC\text{-}II^+SIINFEKL\text{-}H\text{-}2K^+$ population in $CD11c^+$ DC. -: w/o X-ray irradiation; +: w/ X-ray irradiation; Concentration unit: μg/mL.

Cytokine measurement and mechanistic study of DC

We also measured cytokines secreted from DCs. Relative to DCs incubated with cancer cell debris only, secretion of pro-inflammatory cytokines, including IL-6 (**Figure 3.6 a**), IL-12 (**Figure 3.6 b**), and TNF-α (**Figure 3.6 c**), significantly increased when DCs were incubated with AnCHNPs, whereas the level of IL-10 decreased ($p=0.3307$, **Figure 3.6 d**). As a comparison, $CaCl_2$ had no significant impact on maturation and co-stimulatory marker expression nor pro-inflammatory cytokine release. Overall, our experiments suggest that AnCHNPs were able to improve DC processing and presentation of tumor antigens, promote their maturation, and enhance their ability to prime T cells.

Western blotting was performed to understand the impact of AnCHNPs on BMDCs. Relative to controls, BMDCs treated with AnCHNPs showed elevated levels of phosphorated NF-κB and phosphorated IκBα, indicating the activation of the NF-κB pathway. This is consistent with previous observations that elevated $[Ca^{2+}]_{int}$ leaded to elevated maturation, activation and antigen-presentation of DC. This in turn would elevate secretion of pro-inflammatory cytokines such as IL-6, IL-12, and TNF-α.

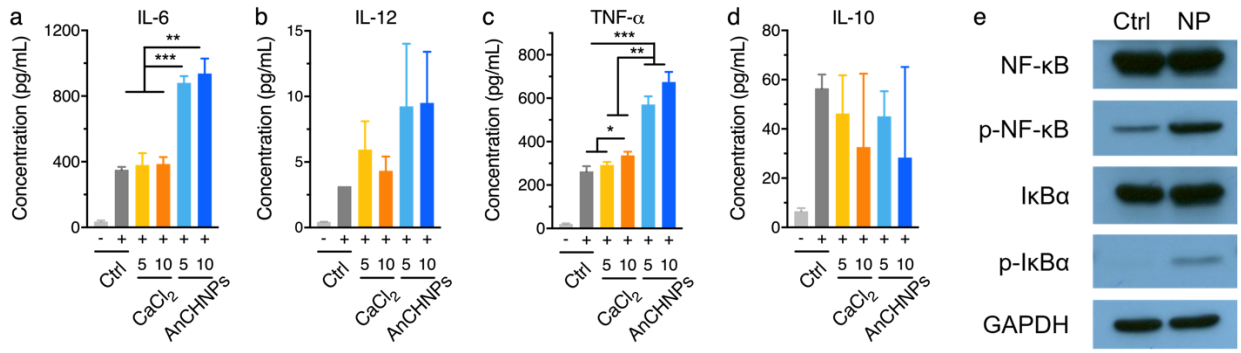

Figure 3.6. Cytokine measurement and western blotting of DC. **a)** Secretion of IL-6 level. **b)** Secretion of IL-12 level. **c)** Secretion of TNF-α level. **d)** Secretion of IL-10 level. **e)** Western blotting of NF-κB pathway. -: w/o X-ray irradiation; +: w/ X-ray irradiation; Concentration unit: μg/mL.

CHAPTER 4

IN VIVO IMMUNE PROFILING

Dendritic cell profiling

We then explored how AnCHNPs would affect DC functions *in vivo*. This was investigated in a B16F10-OVA tumor model. One hour prior to intratumoral administration of AnCHNPs, radiation (10 Gy) was applied to tumors to trigger antigen release. Mice were euthanized on Day 3 or 7; tumors, spleens and tumor-draining lymph nodes (TDLNs) were harvested for flow cytometric analysis (**Figure 4.1 a**). For comparison, carrier only (PBS) and $CaCl_2$ were i.t. injected. Compared to PBS and $CaCl_2$ controls, in mice treated with AnCHNPs, there was a significant increase of $CD11c^+$ abundance in tumors on Day 3 and 7, indicating elevated tumor infiltration of DCs (**Figure 4.1 b**). In particular, populations of MHC-II^+, $CD80^+$, and $CD86^+$ DC cells were significantly increased, indicating AnCHNPs-promoted maturation of DCs. Moreover, AnCHNPs treatment led to a significant increase of $CD11c^+$SIINFEKL-H-$2Kb^+$ cells in both tumors and TDLNs on Day 3, indicating enhanced antigen presentation and cross-presentation abilities (**Figure 4.1 c, d**).

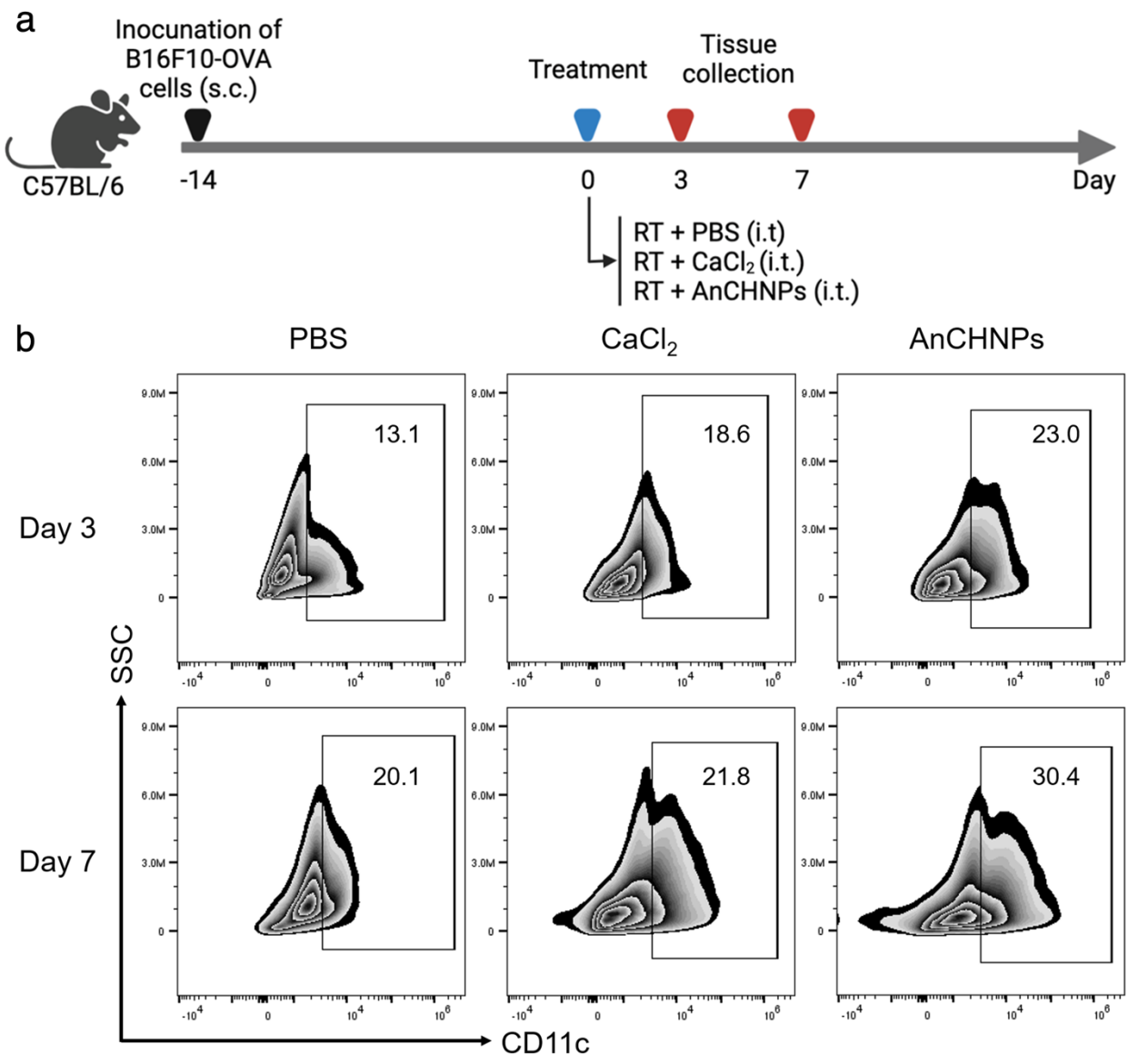
a
Inocunation of
B16F10-OVA
cells (s.c.)
Treatment
Tissue
collection
C57BL/6
-14
0
3
7
Day
RT + PBS (i.t)
RT + CaCl2 (i.t.)
RT + AnCHNPs (i.t.)
b
PBS
CaCl2
AnCHNPs
Day 3
Day 7
SSC
CD11c
13.1
18.6
23.0
20.1
21.8
30.4

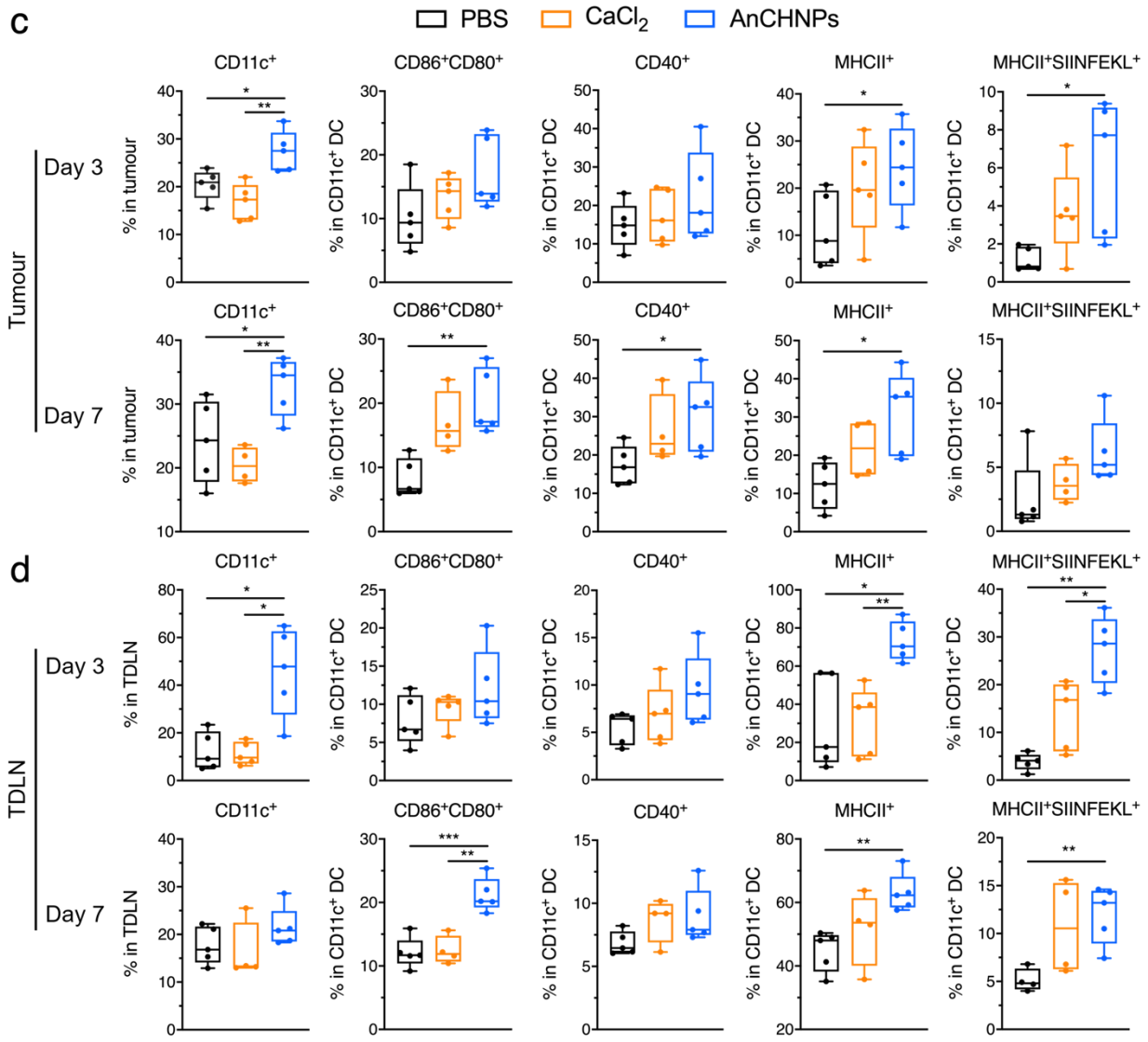

Figure 4.1. *In vivo* dendritic cell profiling. **a)** Scheme of flow cytometry study schedule. **b)** Tumor infiltration of DCs. **c)** DC profiling in tumor on day 3 and day 7; **d)** DC profiling in TDLN on day 3 and day 7.

T cell profiling

We also examined T lymphocytes in tumor and spleen. Compared to the PBS and $CaCl_2$ controls, AnCHNPs significantly increased the frequencies of cytotoxic T cells (CTLs, $CD45^+CD3^+CD8^+$) in tumors on Day 3 and Day 7, along with a reduced level of Tregs

($CD45^+CD3^+CD4^+Foxp3^+$) (**Figure 4.2 a**). Specifically, tumor CTLs/Tregs ratios were increased by around 2 folds on Day 3 and Day 7 relative to the PBS control. Moreover, effector T cells ($CD3^+CD8^+IFN\text{-}\gamma^+$) frequencies were significantly increased in both tumors and spleens (**Figure 4.2 b**). As a comparison, $CaCl_2$ caused little change to the abundances of CTLs and Tregs.

Furthermore, we incubated splenocytes from the three treatment groups with B16F10-OVA cells. The AnCHNPs group showed a significant increase in the level of IFN-γ^+ CTLs, indicating elevated antigen-specific immunity (**Figure 4.2 c**). Conversely, in both $CaCl_2$ and PBS groups splenocytes failed to proliferate when exposed to B16F10-OVA cells.

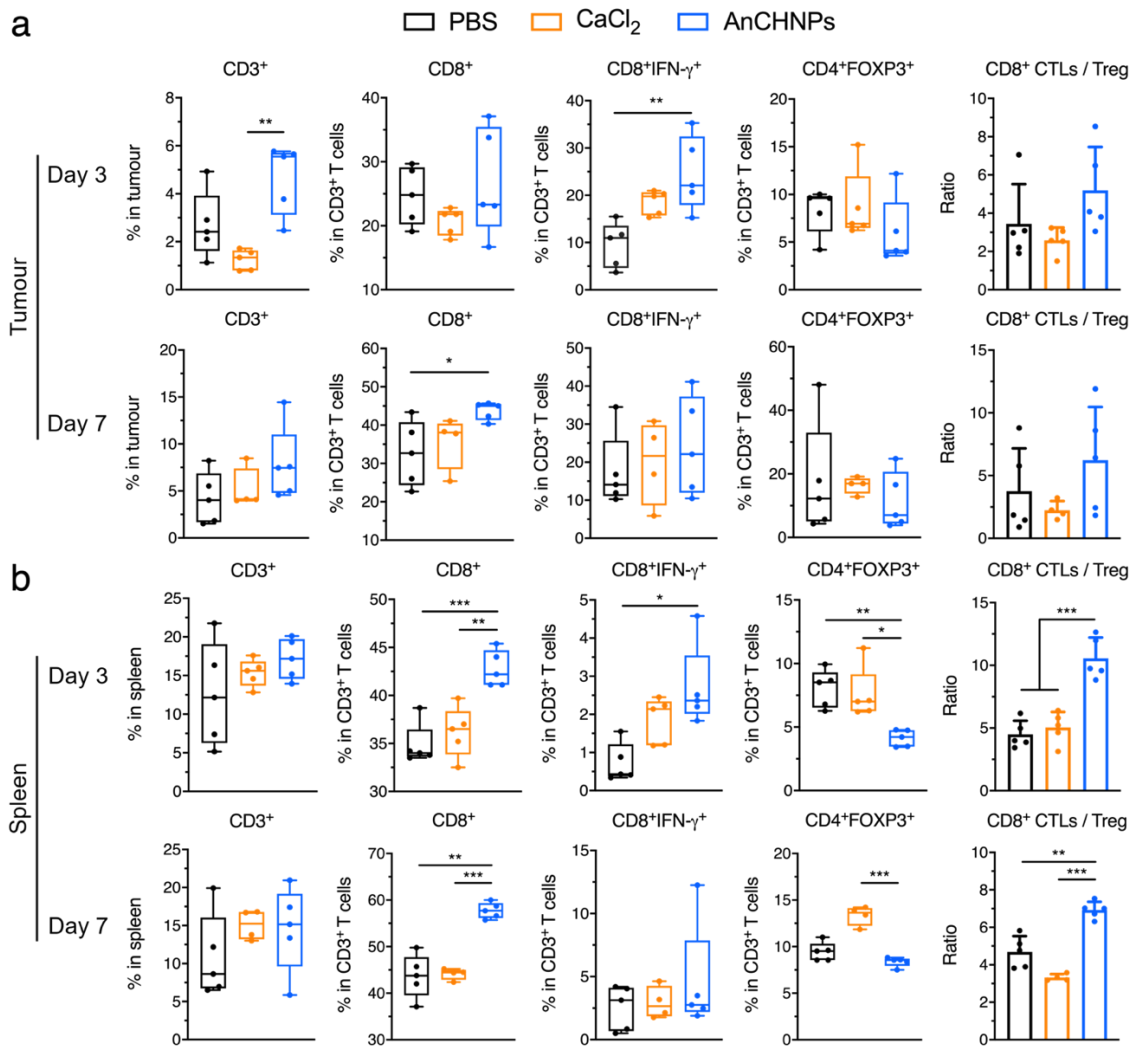

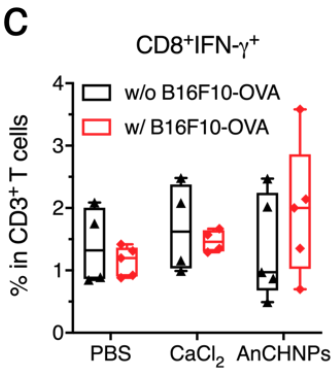

Figure 4.2. *In vivo* T cell profiling. **a)** T cell profiling in tumor on day 3 and day 7. **b)** T cell profiling in spleen on day 3 and day 7. **c)** *Ex-vivo* measurement of effector CTLs in splenocytes.

Cytokine profiling

We also collected blood samples on Day 3, 7 and analyzed cytokine levels in the serum. Relative to the PBS and $CaCl_2$ groups, AnCHNPs-treated animals showed elevated levels of pro-inflammatory cytokines IL-1β (**Figure 4.3 d**), IL-6 (**Figure 4.3 e**), and TNF-α (**Figure 4.3 f**) while a decreased level of anti-inflammatory cytokine IL-10 (**Figure 4.3 c**). Moreover, there was a remarkable increase of IL-12 and IFN-γ on Day 7 (**Figure 4.3 a, b**), corroborating the observation that T lymphocytes' tumor infiltration and activation was boosted when treated with AnCHNPs. Overall, results from these experiments suggest that AnCHNPs can augment anti-tumor immune response initiated by treatments such as RT.

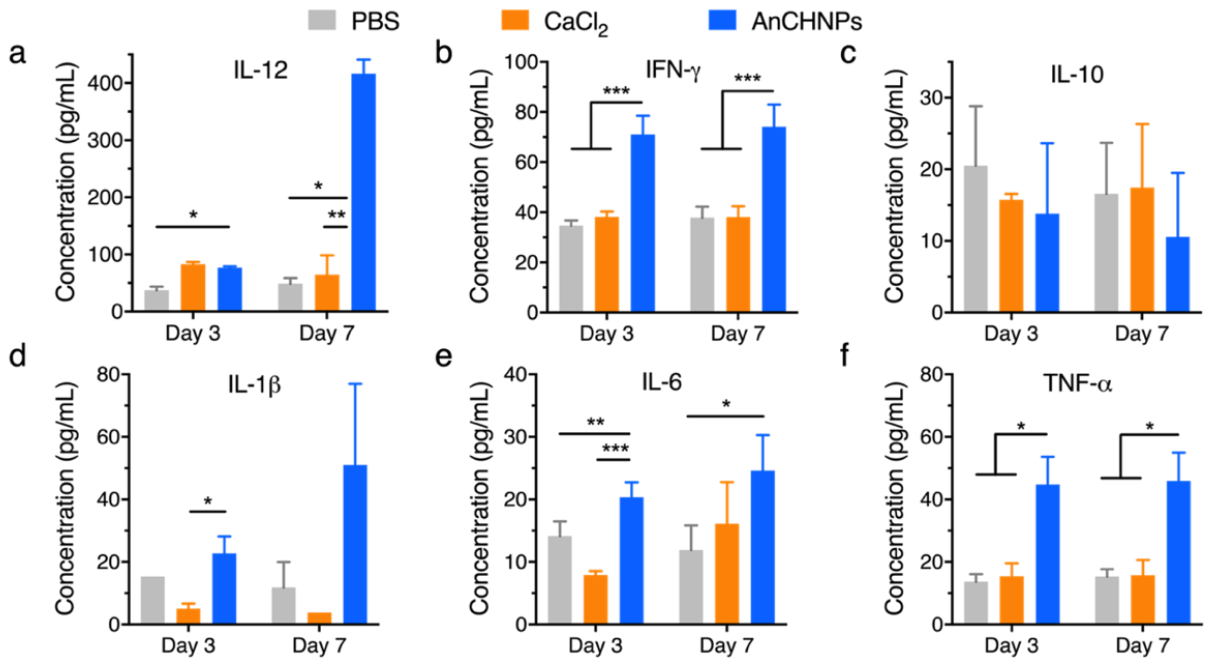

Figure 4.3. *In vivo* cytokine profiling. **a)** IL-12 level on day 3 and 7. **b)** IFN-γ level on day 3 and 7. **c)** IL-10 level on day 3 and 7. **d)** IL-1β level on day 3 and 7. **e)** IL-6 level on day 3 and 7. **f)** TNF-α level on day 3 and 7.

CHAPTER 5

THERAPY STUDY

Therapy study in combination with radiotherapy:

We next evaluated the therapeutic efficacy of AnCNHPs. We tested in the same B16F10-OVA tumor model (**Figure 5.1 a**). AnCHNPs (50 μL, 0.2 mg Ca/kg, in PBS) were i.t. injected on Day 0 and Day 2. Radiation (10 Gy) was applied to tumors one hour prior to AnCHNPs administration, with the rest of the body lead-protected (RT+AnCHNPs; n=5). For comparison, we also tested animals treated with PBS (n=5) and PBS plus irradiation (RT+PBS; n=5), and AnCHNPs only w/o irradiation (AnCHNPs; n=5). Tumors in the PBS group grew rapidly, and all animals died within 2 weeks (**Figure 5.1 b, d**). RT moderately inhibited tumor growth and extended the average survival from 10 days in the PBS group to 16 days (**Figure 5.1 b, c, d**). As a comparison, RT+AnCHNPs significantly improved tumor suppression. A hundred percent of the animals experienced tumor regression in the first three weeks (**Figure 5.1 d**) and all animals remained alive on Day 35 (**Figure 5.1 c**). Notably, AnCHNPs itself at the same calcium dosage failed to slow down tumor growth. Moreover, when anti-CD8 (RT+AnCHNPs+αCD8; n=5) and anti-CD4 (RT+AnCHNPs+αCD4; n=5) antibodies were applied to delete T cells in the body, RT+AnCHNPs failed to retard tumor growth, suggesting that the tumor suppression was mainly mediated by CTLs (**Figure 5.1 b, d**).

Post-mortem hematoxylin/eosin (H&E) staining exhibited large areas of nuclear shrinkage and fragmentation in tumors receiving RT+AnCHNPs. A significantly reduced level of Ki-67

positive staining was found in tumors from the RT+AnCHNPs group relative to the controls, corroborating efficient cancer cell killing (**Figure S5.1, Appendices D**). Meanwhile, no sign of systemic toxicity was observed in normal tissues (**Figure S5.2, Appendices D**).

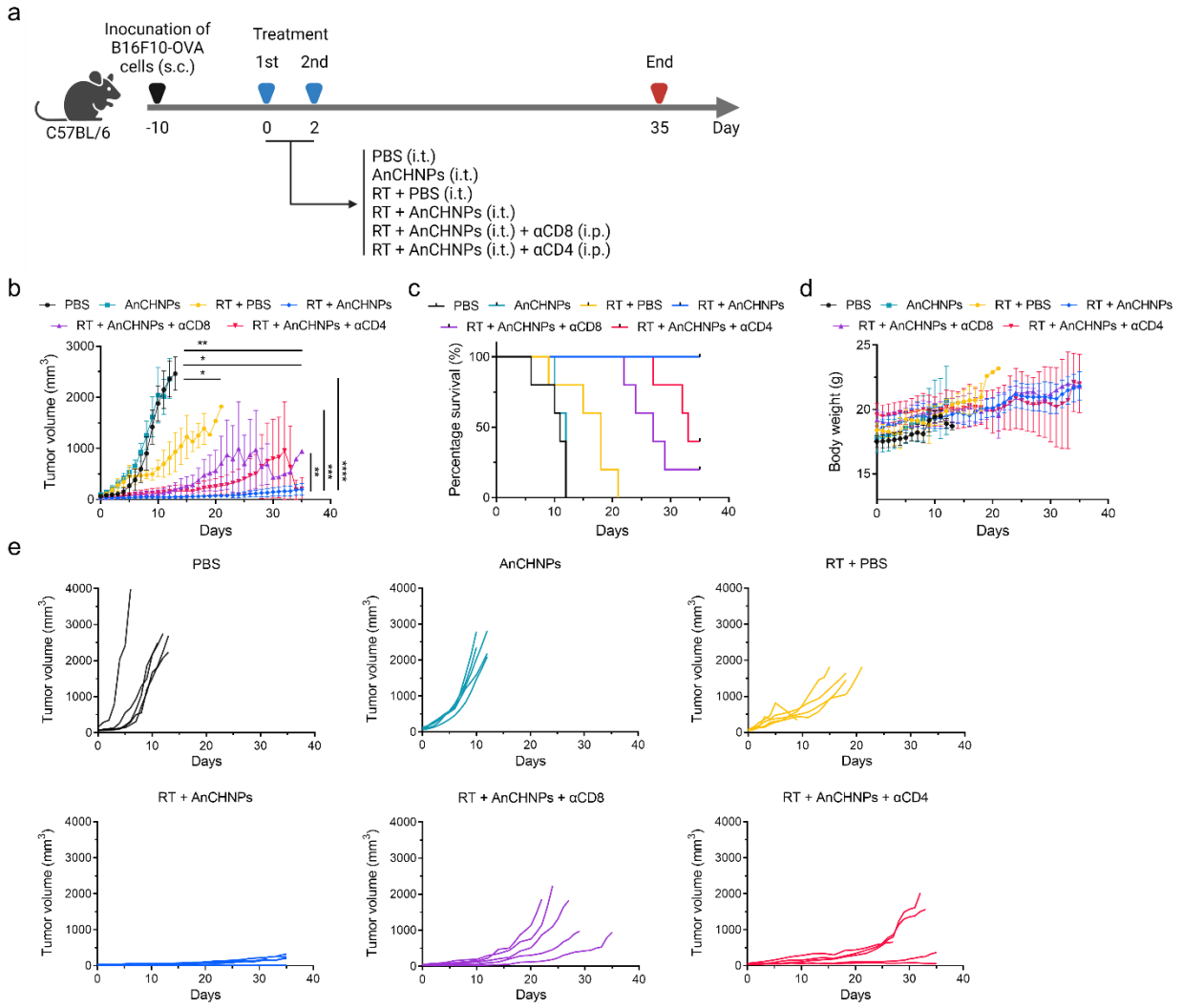

Figure 5.1. Therapy study on B16F10-OVA tumor model - Radiotherapy. **a)** Scheme of therapy study on B16F10-OVA tumor model. **b)** B16F10-OVA tumor growth curve. **c)** Mice percentage survival curve. **d)** Individual mice tumor growth curve.

We repeated the study with radiotherapy in M49 bladder carcinoma tumor model (**Figure 5.2 a**). Similar as observed in previous B16F10-OVA model, AnCHNPs were able to enhance RT-based tumor suppression (**Figure 5.2 b, e**). At end point, 60% of mice remained alive compared to the average survival of 40 days in RT group and 17 days in PBS control group (**Figure 5.2 c**). Meanwhile, all animals were well tolerated to combination therapy with AnCHNPs, showing no acute toxicity or body weight drop throughout the experiment (**Figure 5.2 d**).

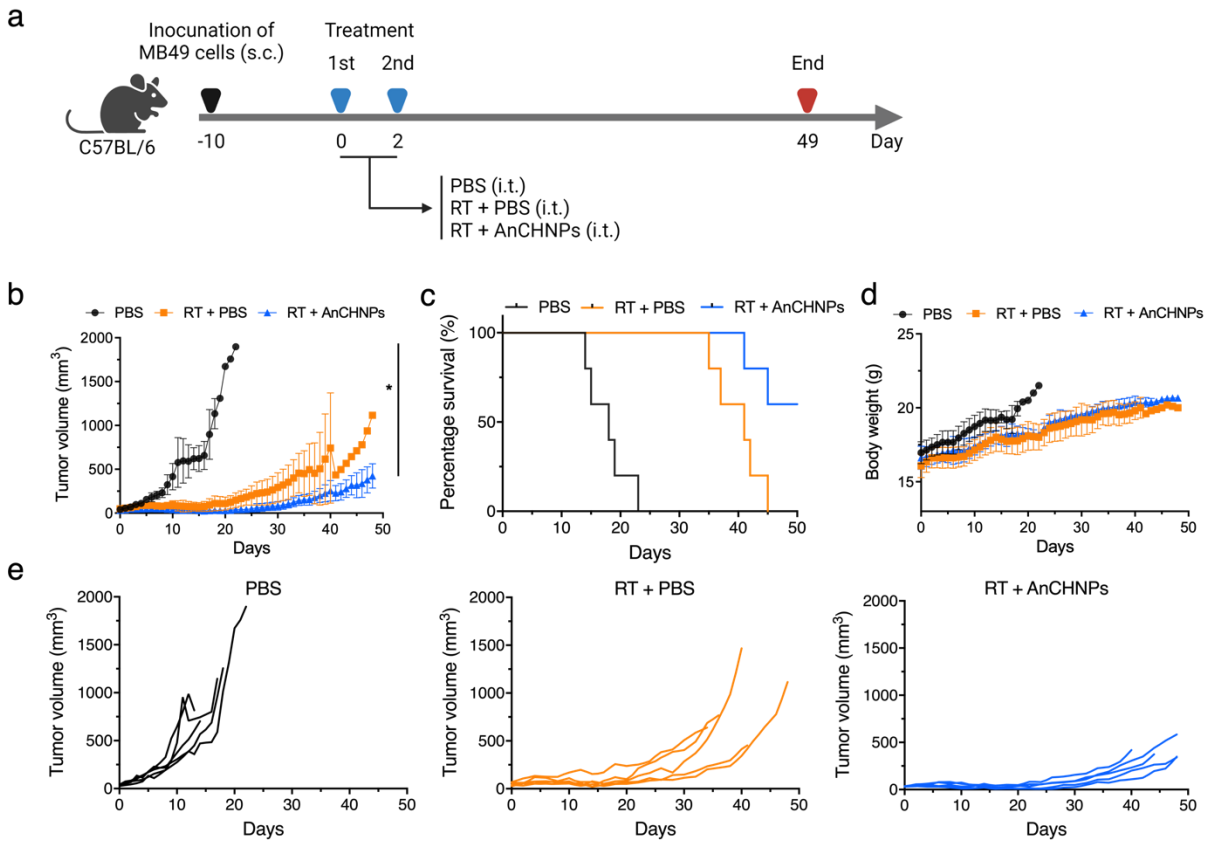

Figure 5.2. Therapy study on MB49 tumor model - Radiotherapy. **a)** Scheme of therapy study on MB49 tumor model. **b)** MB49 tumor growth curve. **c)** Mice percentage survival curve. **d)** Mice body weight curve. **e)** Individual mice tumor growth curve.

Therapy study in combination with chemotherapy:

We went on to test AnCHNPs as combination therapy with other therapy strategies such as chemotherapy in the same B16F10-OVA tumor model (**Figure 5.3 a**). Carboplatin (CP, n=5, 40 mg/kg, i.p.) was applied to mice as chemotherapy drug to induce immunogenic cell death which moderately inhibited tumor growth (**Figure 5.3 b**). As comparison, CP+AnCHNPs significantly enhanced tumor growth suppression and prolonged average survival of mice from 15 days of CP treated group to 23 days of CP+AnCHNPs treated group (**Figure 5.3 c, e**). Meanwhile, these treatments caused little systematic toxicity as there was no acute body weight loss during these experiments (**Figure 5.3 d**).

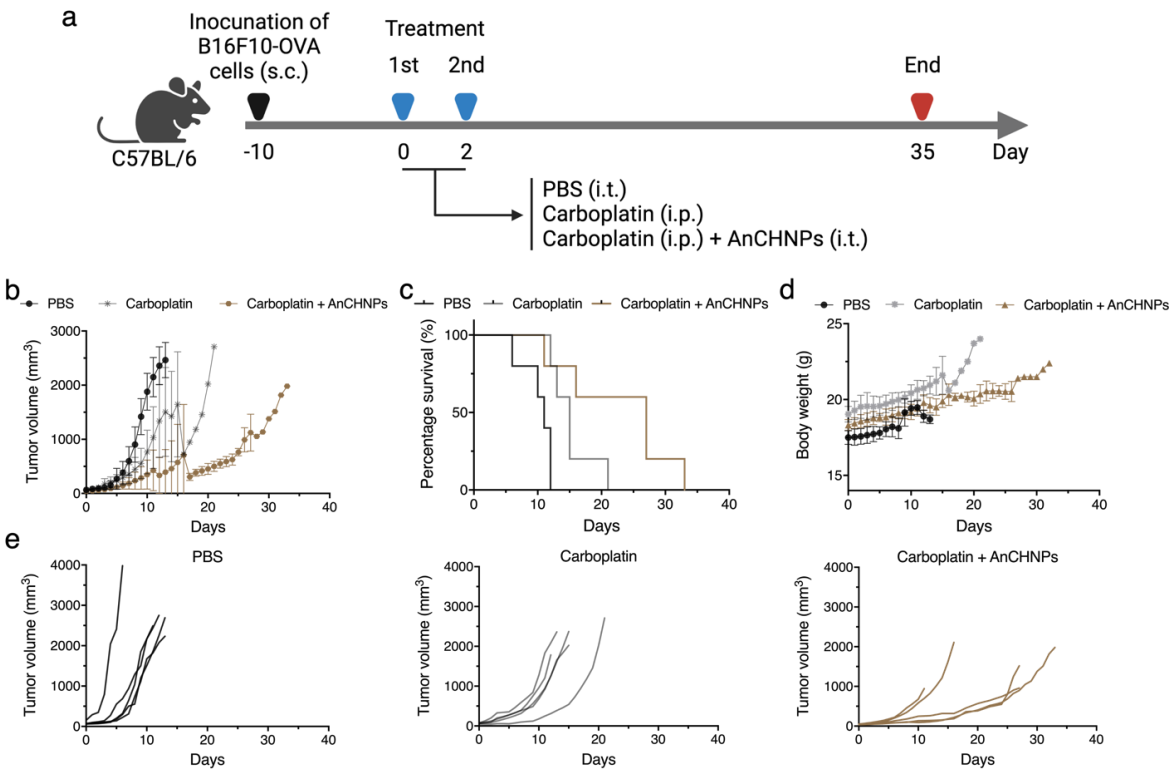

Figure 5.3. Therapy study on B16F10-OVA tumor model - Chemotherapy. **a)** Scheme of therapy study on B16F10-OVA tumor model. **b)** B16F10-OVA tumor growth curve. **c)** Mice percentage survival curve. **d)** Mice body weight curve. **e)** Individual mice tumor growth curve.

Therapy study in combination with immunotherapy:

We also tested AnCHNPs together with immunotherapy in the same B16F10-OVA tumor model (**Figure 5.4 a**). Immune check point inhibitor anti-PD-1 (αPD-1, 10 mg/kg, 100 μL in PBS, n=5, i.p.) was injected into mice on Day 0 and Day 2. AnCHNPs (αPD-1+AnCHNPs, n=5) were i.t. injected on Day 0 and Day 2. Also, Radiation (10 Gy) was applied to tumors one hour prior to AnCHNPs administration, with the rest of the body lead-protected (RT+αPD-1, n=5; RT+αPD-1+AnCHNPs; n=5). Combination therapy with AnCHNPs showed enhanced tumor growth suppression with both αPD-1 and RT+αPD-1 treatments, and mice survival were prolonged to 12 days and 27 days compared with αPD-1 treatment only (10 days) and RT+αPD-1 treatment (23 days) respectively (**Figure 5.4 b**). Meanwhile, all animals were well tolerated to combination therapy with AnCHNPs (**Figure 5.4 c**).

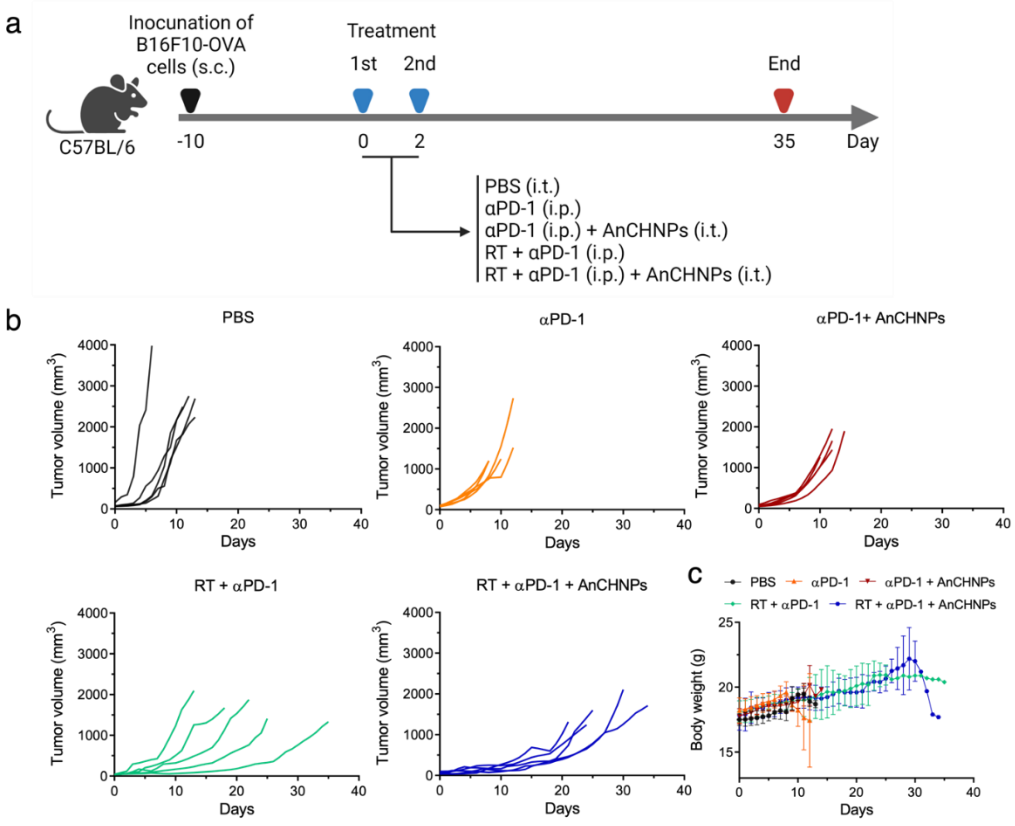

Figure 5.4. Therapy study on B16F10-OVA tumor model - Immunotherapy. **a)** Scheme of therapy study on B16F10-OVA tumor model. **b)** Individual mice tumor growth curve. **c)** Mice body weight curve.

Therapy study on B16F10 tumor model:

We repeated the study with immunotherapy in another transplanted tumor model B16F10 murine melanoma (**Figure 5.5 a**). Of note, B16F10 is more poorly immunogenic model and is refractory to RT. In this model, AnCHNPs were also able to enhance immunotherapy-based tumor suppression (**Figure 5.5 b, e**). Average survival of mice treated with αPD-1+AnCHNPs was increased to 11 days compared to αPD-1 treatment only group of 9 days and PBS group of 8 days (**Figure 5.5 c**). Meanwhile, all animals were well tolerated to combination therapy with AnCHNPs, showing no acute toxicity or body weight drop throughout the experiment (**Figure 5.5 d**).

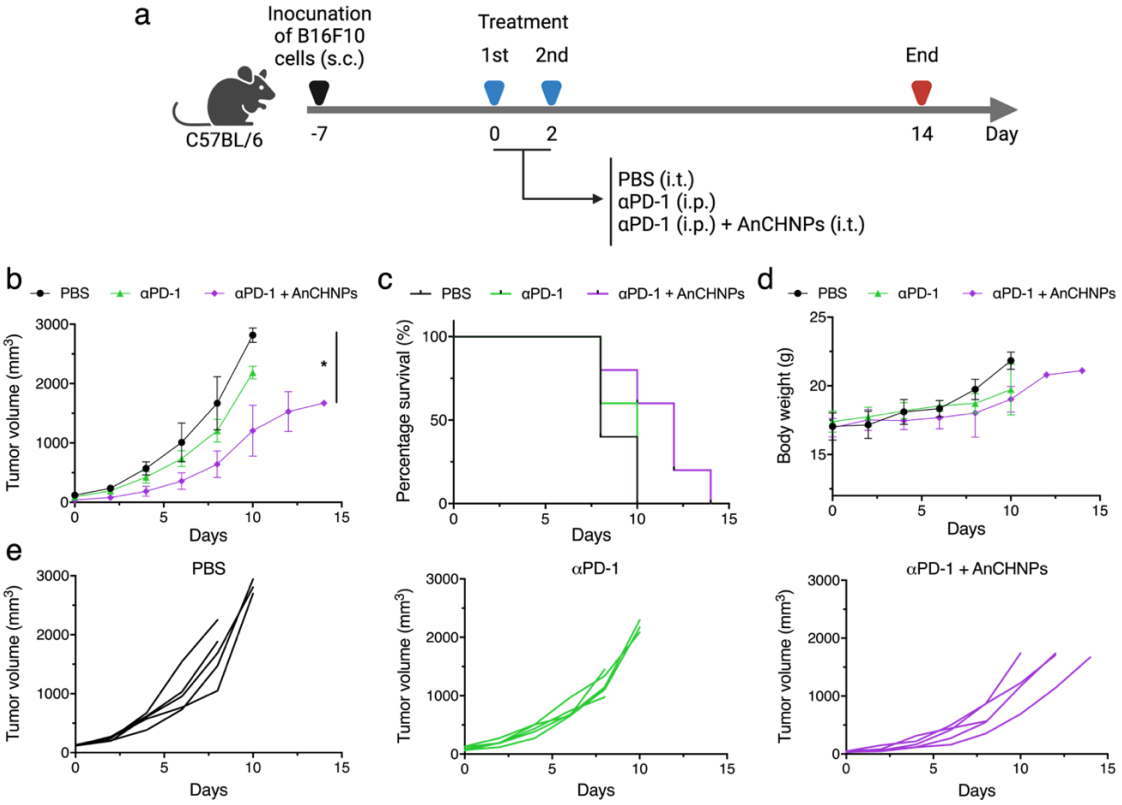

Figure 5.5. Therapy study on B16F10 tumor model. **a)** Scheme of therapy study on B16F10 tumor model. **b)** B16F10 tumor growth curve. **c)** Mice percentage survival curve. **d)** Mice body weight curve. **e)** Individual mice tumor growth curve.

Overall, our results confirmed the efficacy and safety of AnCHNPs in enhancing RT-based tumor control. The enhancement was largely mediated by CTLs, which is consistent with the immune profiling results.

CHAPTER 6

BARIUM TUNGSTATE NANOPARTICLES TO ENHANCE RADIATION THERAPY AGAINST CANCER[1]

[1] Renjie Wang, Zhengwei Cao, Lan Wei, Lin Bai, Hui Wang, Shiyi Zhou, Shuyue Zhan, Bin Ji, Zibo Li, Shi Gao, Jin Xie, Qingjie Ma. *Nanomedicine: Nanotechnology, Biology, and Medicine* 28 (2020) 102230. Reprinted here with permission of the publisher.

Abstract

In this chapter, we also investigated another element barium from second column same as calcium, as potential high-Z nanoparticles for radiosensitizer in radiotherapy for cancer treatment. High-Z nanoparticles have emerged as a novel type of radiosensitizers due to their relatively large X-ray cross-section and ability to enhance radical production under irradiation. Recently, $CaWO_4$ nanoparticles have been prepared and their potential as a radiosensitizer has been demonstrated. Herein, we investigated $BaWO_4$ nanoparticles as a novel type of alkaline-earth metal tungstate radiosensitizer for radiotherapy (RT). We synthesized $BaWO_4$ nanoparticles using hydrothermal reaction and coated them with polyvinylpyrrolidone (PVP). We found that $BaWO_4$ nanoparticles could more efficiently enhance hydroxyl radical production under irradiation than $CaWO_4$ nanoparticles. When tested in vitro, $BaWO_4$ nanoparticles showed lower toxicity than $CaWO_4$ nanoparticles in the absence of irradiation, but induced more significant oxidative stress under irradiation. When tested in vivo, $BaWO_4$ nanoparticles led to more efficient tumor inhibition without causing systemic toxicity. Overall, our results suggest that $BaWO_4$ nanoparticles can efficiently enhance RT and hold great potential as a novel type of radiosensitizing agent.

Introduction

RT remains a mainstay treatment option for cancer.[1-5] During RT, high-energy beams are delivered to tumors to induce cancer cell death. Despite advances in radiation delivery, normal tissue toxicity is inevitable, which limits radiation doses and treatment outcomes.[6] To improve, radiosensitizers are often administered during RT.[7-9] Conventional radiosensitizers are chemotherapeutics such as fluorouracil, gemcitabine and cisplatin, which may cause severe

systematic toxicity.[10] There is a growing interest of developing high-Z nanoparticle radiosensitizers, which afford large X-ray cross-section and can enhance production of photoelectrons and Auger electrons during irradiation.[11] Previously, gold nanoparticles have been extensively investigated as radiosensitizers.[12-15] More recently, Gd-bound silica nanoparticles[16-18] and HfO_2 nanoparticles have entered clinical trials.[19-22]

Alkaline-earth metal tungstates represent another class of materials that hold great promise in radiosensitization. Alkaline-earth metal tungstates have large X-ray cross-section and relatively low toxicity, and they have been widely used as scintillation materials.[23] $CaWO_4$, for instance, shows strong photoelectric effects and radio-luminescence, and has been investigated for applications such as dosimetry[24, 25] and biomedical imaging.[26] Very recently, Jo et al. assessed $CaWO_4$ nanoparticles as a radiosensitizer for cancer treatment.[27] So far, however, there have been few attempts of exploring other alkaline-earth metal tungstates in the context of RT. Herein, we synthesized $BaWO_4$ nanoparticles and assessed their potential as a novel radiosensitizer. $BaWO_4$ contains a heavier cation than $CaWO_4$. We hypothesize that $BaWO_4$ nanoparticles can outperform $CaWO_4$ nanoparticles with regard to enhancing radical production and RT outcomes (**Figure 6.1**). Briefly, we synthesized $BaWO_4$ nanoparticles through a hydrothermal reaction and coated the particles with a layer of PVP. PVP is a water-soluble polymer that has been approved by FDA for many pharmaceutical uses. PVP has also been exploited as a coating material for nanoparticles to improve their bio-compatibility and colloidal stability.[28, 29] In this study, we first tested radical production under irradiation with solutions containing $BaWO_4$ or $CaWO_4$ nanoparticles. We then tested, with 4T1 cells (murine breast cancer), whether $BaWO_4$ nanoparticles can elevate radiation-induced oxidative stress and cell death. Lastly, we assessed whether $BaWO_4$ nanoparticles can improve RT efficacy relative to $CaWO_4$ nanoparticles in 4T1 xenograft models.

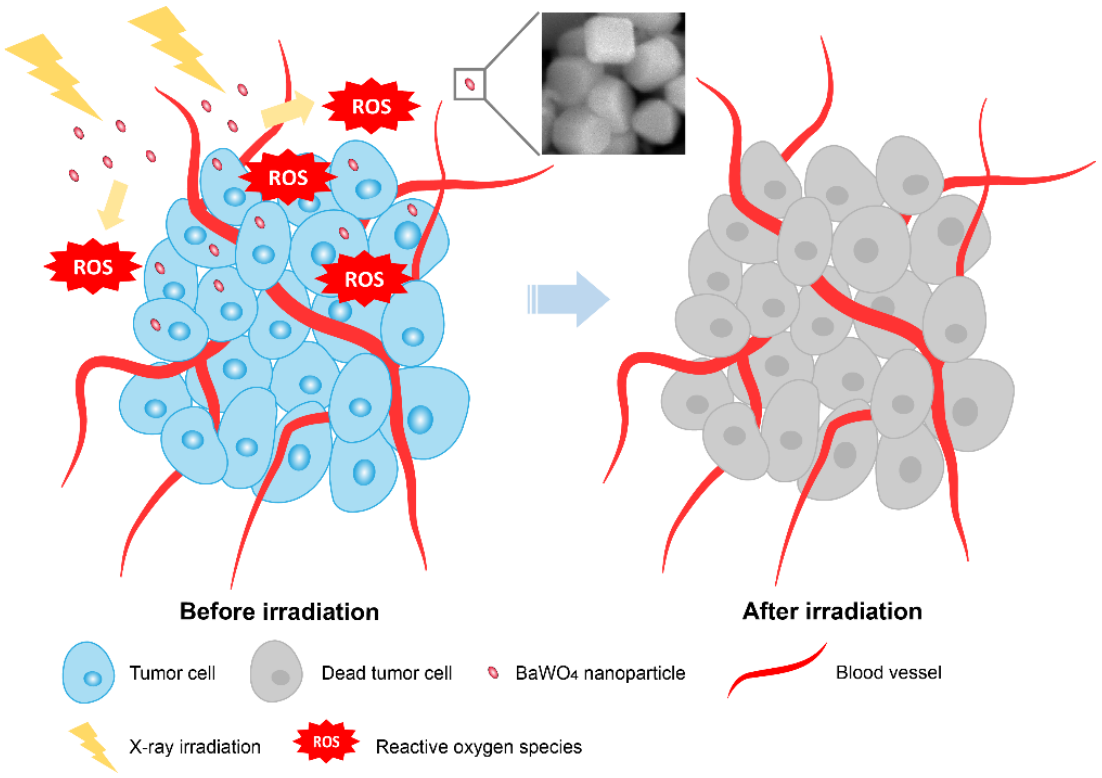

Figure 6.1. Schematic illustration of PVP-$BaWO_4$ nanoparticle enhanced RT against tumors.

Methods

Chemicals

Barium chloride ($BaCl_2$, anhydrous, ≥97%, Fisher Scientific), calcium chloride ($CaCl_2$, anhydrous, ≥97%, Millipore Sigma), sodium tungstate dihydrate ($Na_2WO_4 \cdot 2H_2O$, ≥99%, Fisher Scientific), hexadecyltrimethylammonium bromide (CTAB, ≥99%, Millipore Sigma), polyvinylpyrrolidone (PVP, MW 360,000, Millipore Sigma), thiazolyl blue tetrazolium bromide (MTT, ≥97.5%, HPLC, Millipore Sigma), 3'-(p-aminophenyl) fluorescein (APF, Life Technologies), singlet oxygen sensor green (SOSG, Life Technologies), superoxide dismutase assay kit (SOD, Cayman Chemical), cyclohexane (C_6H_{12}, anhydrous, 99.5%, Millipore Sigma), 1-hexanol ($CH_3(CH_2)_5OH$, anhydrous, ≥99%, Millipore Sigma), chloroform ($CHCl_3$, ≥99.8%, Fisher

Scientific), ethanol (C_2H_5OH, 200 Proof, KOPTEC), dimethylformamide (DMF, ≥99.9%, Millipore Sigma), methanol (CH_3OH, ≥99.9%, Fisher Scientific), phosphate buffer saline (PBS, pH 7.2), HCl (J.T. Baker, 36.5-38%), Milli-Q Water (H_2O, 18.2 MΩ.cm@25℃). All reagents were used as received.

Synthesis of $BaWO_4$/$CaWO_4$ nanoparticles

The $BaWO_4$ nanoparticles were synthesized through a modified micro-emulsion method. In a typical synthesis, 2 mmol of CTAB was added into a solvent mixture containing 20 mL of cyclohexane and 2 mL of 1-hexanol. The solution was heated up to 70 ℃ until it became transparent (solution 1). Then 0.4 mmol of $Na_2WO_4 \cdot 2H_2O$ was dissolved in 0.6 mL of Milli-Q H_2O (solution 2). Another 0.4 mmol of $BaCl_2$ was dissolved in a mixture containing 0.564 mL Milli-Q H_2O and 0.036 mL of 0.1 M HCl (solution 3). Solution 2 and 3 were injected immediately into solution 1 and the resulting mixture was kept under vigorously stirring. After about 1 minute, the solution was transferred into a Teflon-lined autoclave, which was then heated up to 160 ℃. After 24 h, the autoclave was cooled down to room temperature and the products were collected by centrifugation at 10,000 rpm and washed by ethanol and chloroform for 5 times to remove residual CTAB, cyclohexane, and 1-hexanol. The $CaWO_4$ NPs were synthesized via a similar protocol using $CaCl_2$ instead of $BaCl_2$ as the alkaline precursor.

PVP coating for $BaWO_4$/$CaWO_4$ nanoparticles

As-synthesized $BaWO_4$ and $CaWO_4$ nanoparticles were coated with PVP using a modified protocol.[30] Briefly, 10 mg of purified $BaWO_4$/$CaWO_4$ nanoparticles were dispersed in 3.0 mL Milli-Q H_2O by sonication. 10 mL PVP in DMF (100 mg/mL) was added to the nanoparticle suspension. The mixture was kept under vigorous stirring for 30 min and sonicated for 30 min. The resulting emulsion was subjected to centrifugation at 10,000 rpm for 10 min and washed with

methanol 3 times to remove DMF and PVP residuals. The resulting PVP-coated $BaWO_4$/PVP-$CaWO_4$ nanoparticles (PVP-$BaWO_4$/PVP-$CaWO_4$ NPs) can be dispersed well in aqueous solutions.

Characterizations of PVP-$BaWO_4$/PVP-$CaWO_4$ NPs

The nanoparticle size was characterized by Transmission Electron Microscope (TEM, FEI Tecnai20, 200 kV). The morphology and EDS element mapping of nanoparticles were assessed by Scanning Electron Microscope (SEM, FEI Teneo) equipped with an EDAX EDS system. Nanoparticle crystallinity was assessed by XRD on a PANalytical X'Pert PRO Powder X-ray Diffractometer with Cu Kα radiation (λ = 1.5406 Å). Nanoparticle coating was verified by Fourier transform infrared (FT-IR) (Nicolet iS10, Thermo Scientific).

Measurement of singlet oxygen ($^1O_2$) in solutions

The singlet oxygen level change was analyzed by SOSG assay according to the vendor's protocol.[31] Two different concentrations of PVP-$BaWO_4$ or PVP-$CaWO_4$ NPs (24 and 48 μM) in PBS were prepared. PBS alone was studied as a control. A mini-X X-ray tube (Amptek Inc.) was used for the study and it was operated at 50 kV and 70 μA. $^1O_2$ levels of all groups before and after 5 Gy X-ray irradiation were assessed by measuring SOSG fluorescence (excitation/emission: 504/525 nm) using a microreader.

Measurement of hydroxyl radicals in solutions

Hydroxyl radical production in the presence of nanoparticles was characterized by APF assay according to the vendor's protocol.[31] PVP-$BaWO_4$ or PVP-$CaWO_4$ NPs were dispersed in PBS (48 μM) containing 5 μM APF. PBS alone was studied as a control. Hydroxyl radical levels of all groups before and after 5 Gy X-ray irradiation were detected by measuring APF fluorescence (excitation/emission: 490/515 nm) using a microreader.

Cell culture

4T1 breast cancer cells were used for *in vitro* and *in vivo* studies. Cells were grown in RPMI 1640 medium supplemented with 10% FBS, 100 units/mL of penicillin, and 100 μg/mL streptomycin (ATCC). The cells were maintained in a humidified, 5% carbon dioxide (CO_2) at 37 °C.

Intracellular radical measurement

4T1 cells (10^4 cells per well) were seeded in a 96-well plate (Corning) and cultured for 12 hrs. The incubation medium was removed and replaced with fresh medium containing PVP-$BaWO_4$ or PVP-$CaWO_4$ NPs (24 μM). For controls, nanoparticle-free fresh medium was added to the wells. For SOSG assay, cells after 4 or 24 h incubation with the nanoparticles were washed with PBS and incubated in 100 μL 5 μM SOSG in PBS. Singlet oxygen levels before and after 5 Gy X-ray irradiation were detected by measuring fluorescence (excitation/emission: 504/525 nm) on a microreader. For APF test, 100 μL PBS solution containing 5 μM APF was added to the plate after cell washing. Hydroxyl radical levels before and after 5 Gy X-ray irradiation were detected by measuring fluorescence (excitation/emission: 490/515 nm) on a microreader. SOD assay was performed according to vendor's protocol by measuring absorbance at 450 nm.

Cell viability test

Cells were seeded in a 96-well plate (Corning) (10^4 cells per well) and cultured for 12 h. For viability in the absence of X-ray irradiation, cells were incubated with culture medium containing PVP-$BaWO_4$ or PVP-$CaWO_4$ NPs of different concentrations (3, 6, 12, 24, 48, 96, 192 μM). MTT assays were performed 24 h later. For tests with nanoparticles plus irradiation, PVP-$BaWO_4$ or PVP-$CaWO_4$ NPs were incubated with cells at 24 μM for 4 h, followed by 5 Gy X-ray

irradiation. Cell viability was measured 20 h later by MTT assays. For controls, fresh medium containing no nanoparticles was tested.

In vivo therapy

Animal studied were performed according to protocols approved by the Institutional Animal Care and Use Committee (IACUC) of China–Japan Union Hospital of Jilin University and the University of Georgia. One million 4T1 cells were inoculated subcutaneously to both flanks of BALB/c mouse. When tumor sizes reached 100 mm^3, each tumor was injected with 50 μL PVP-$BaWO_4$ or PVP-$CaWO_4$ NPs dispersed in PBS (5 mg/kg). For control, 50 μL PBS was injected. 1 h after the injection, the tumors were irradiated by 10 Gy radiation on an X-RAD 320 system. Tumor dimensions were measured every three days.

Results

$BaWO_4$ nanoparticles were synthesized through a hydrothermal reaction. Briefly, CTAB was dissolved in cyclohexane/1-hexanol, and was added into an aqueous solution containing $BaCl_2$ and Na_2WO_4. The resulting mixture underwent vigorous stirring at 70 ℃ for 1 minute before transferred to a Teflon-lined autoclave. The autoclave was heated at 160 ℃ for 24 h, and then cooled down to room temperature. The products were collected by centrifugation. Transmission electron microscopy (TEM) and scanning electron microscopy (SEM) showed that $BaWO_4$ nanoparticles had an average size of 318 ± 72 nm (**Figure 6.2 a, b**). Energy-dispersive X-ray spectroscopy (EDS) analysis found element Ba, W, and O in the nanoparticles (**Figure 6.2 c**). X-ray diffraction (XRD) confirmed that the product was $BaWO_4$ (**Figure 6.2 d**, index # 01-079-6949). For comparison, $CaWO_4$ nanoparticles were synthesized through a similar recipe, except

using $CaCl_2$ as the alkaline earth metal precursor. EDS and XRD confirmed that the chemical composition of the resulting nanoparticles was $CaWO_4$ (**Figure 6.2 c, d**, index # 01-083-6134).

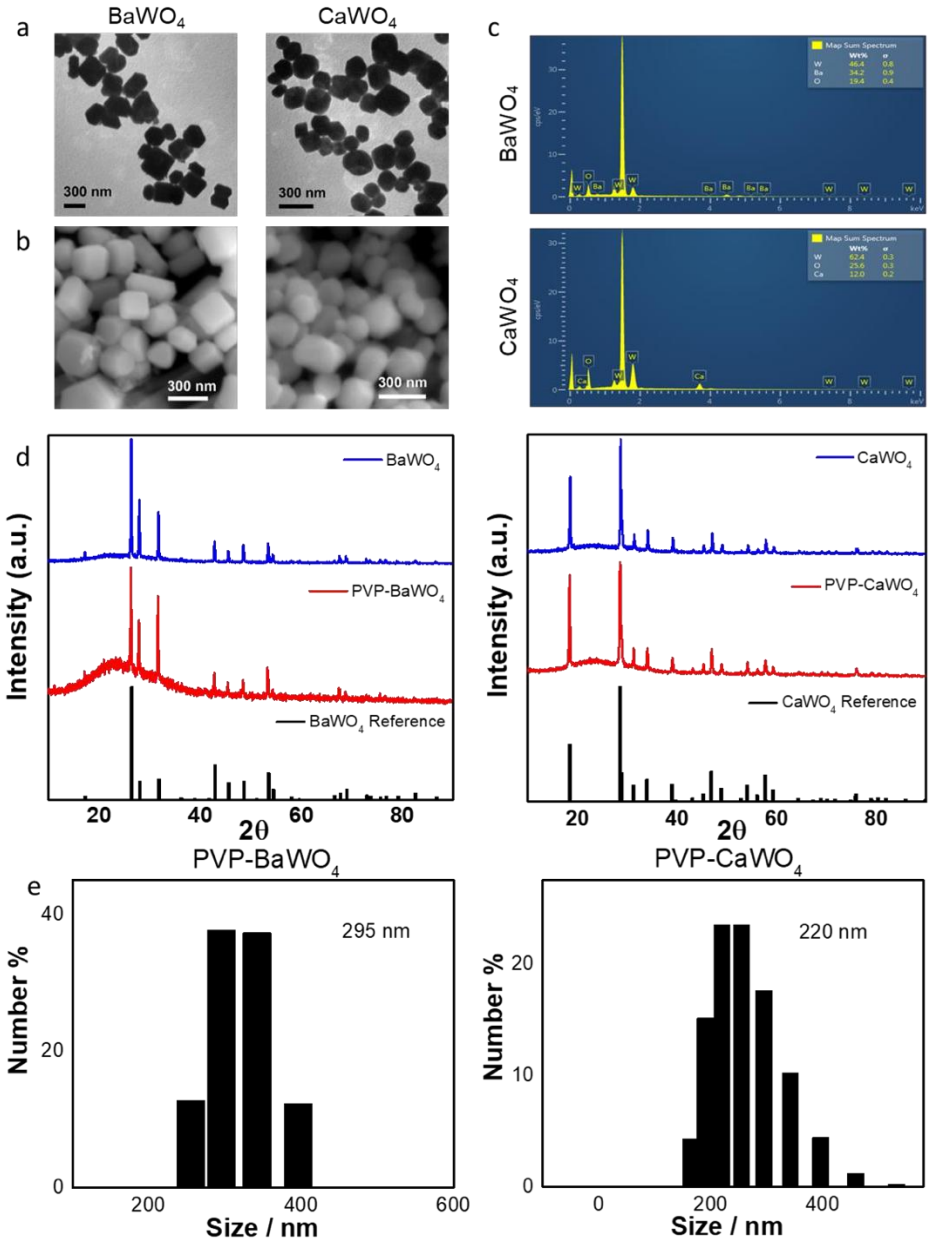

Figure 6.2. Characterizations. (a) TEM images of PVP-$BaWO_4$ and PVP-$CaWO_4$ nanoparticles; (b) SEM images of PVP-$BaWO_4$ and PVP-$CaWO_4$ nanoparticles; (c) EDS analysis of PVP-$BaWO_4$ and PVP-$CaWO_4$ nanoparticles; (d) XRD spectra of PVP-$BaWO_4$ and PVP-$CaWO_4$ nanoparticles; (e) DLS analysis of PVP-$BaWO_4$ and PVP-$CaWO_4$ nanoparticles.

Bare $BaWO_4$ nanoparticles were easily aggregated in aqueous solutions. To improve colloidal stability, the as-synthesized $BaWO_4$ and $CaWO_4$ nanoparticles were coated with PVP. This was achieved by incubating $BaWO_4$ or $CaWO_4$ nanoparticles and PVP in DMF/H_2O solution, and removing the extra PVP by washing with methanol for 3 times. The resulting nanoparticles can be well suspended in water or PBS (**Figure 6.3 a**). The successful coating was confirmed by FT-IR analysis, which found with both PVP-$BaWO_4$/$CaWO_4$ nanoparticles peaks at around 3400, 2900, 1500 and 1300, and 1000 cm^{-1}, corresponding to O-H, C-H, C=O and C-N stretching, respectively (**Figure 6.3 b**). The coating did not affect the crystallinity of the nanoparticles, as indicated by XRD analysis (**Figure 6.2 d**). Dynamic light scattering (DLS) found that the hydrodynamic sizes of PVP-$BaWO_4$ and $CaWO_4$ nanoparticles were 295 nm and 220 nm, respectively (**Figure 6.2 e**). Zeta potential analysis showed that the nanoparticle surface charge was close to neutral. We also analyzed nanoparticle size changes in both acidic and neutral solutions (pH=5.0 and 7.4) over 24 h incubation. No significant size change was observed, suggesting good colloidal stability rendered by the PVP coating.

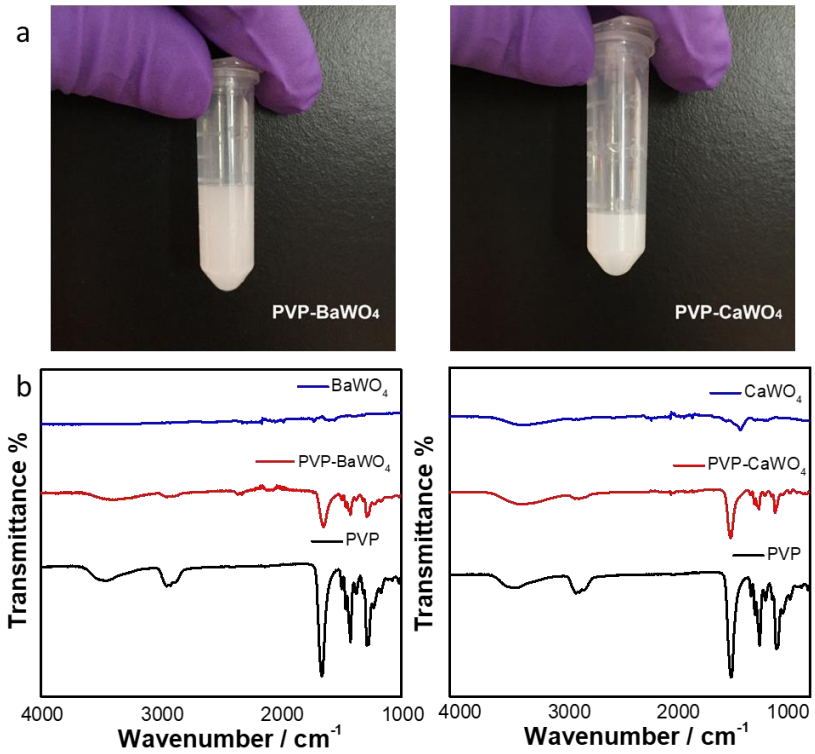

Figure 6.3. (a) Photographs of PVP-$BaWO_4$ and PVP-$CaWO_4$ nanoparticles suspended in PBS; (b) FT-IR spectra of PVP-$BaWO_4$ and PVP-$CaWO_4$ nanoparticles.

We then analyzed how PVP-$BaWO_4$ or $CaWO_4$ nanoparticles affected radical production. Briefly, PVP-$BaWO_4$ or $CaWO_4$ nanoparticles were dispersed in PBS (24 or 48 μM, W concentration, the same below), and irradiated by 5 Gy X-ray. The radical levels were measured by SOSG and APF assays, which detect singlet oxygen and hydroxyl radicals, respectively. The singlet oxygen level barely changed when either $BaWO_4$ or $CaWO_4$ nanoparticles were present (**Figure 6.4 a**). Meanwhile, the amount of hydroxyl radical was drastically increased in the presence of tungstate nanoparticles, and much more so with $BaWO_4$ nanoparticles (**Figure 6.4 b**). Specifically, relative to RT only, the APF fluorescence was increased by 6.2-fold with 48 μM $BaWO_4$ plus radiation (denoted as $BaWO_4$+RT), compared to a 3.0-fold increase with $CaWO_4$+RT.

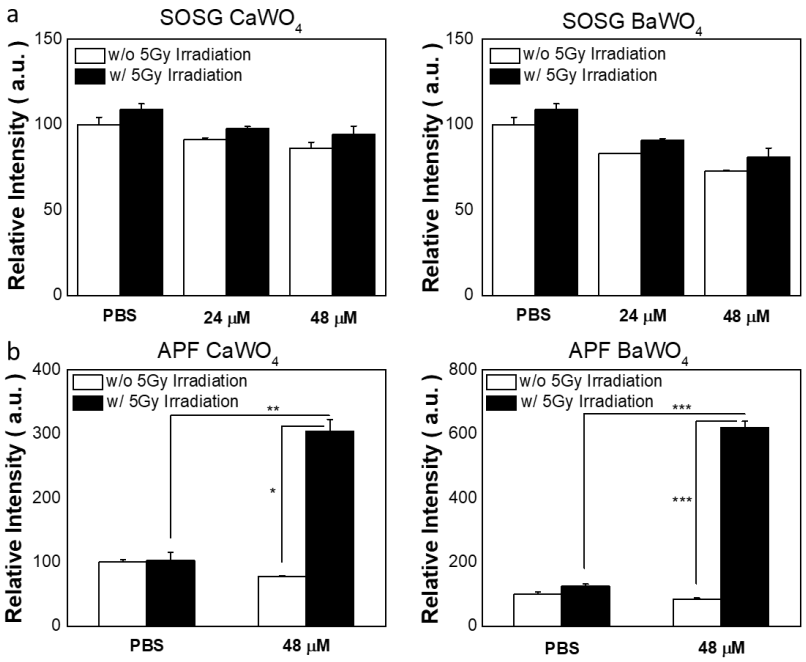

Figure 6.4. Radical production under irradiation in solutions. (a) SOSG and (b) APF assays with solutions containing PVP-$CaWO_4$ and PVP-$BaWO_4$ nanoparticles. *, P<0.05; **, P<0.01; ***, P<0.001. Fluorescence was examined to measure radical levels in the presence of PVP-$CaWO_4$ or PVP-$BaWO_4$ nanoparticles with or without 5 Gy X-ray irradiation.

The cytotoxicity of PVP-$BaWO_4$ or $CaWO_4$ nanoparticles was first assessed in the absence of X-ray radiation. This was evaluated by incubating PVP-$BaWO_4$ or $CaWO_4$ nanoparticles of different concentrations (0-192 μM) with 4T1 cells, and subjecting the cells to MTT assays at 24 h. It was found that PVP-$BaWO_4$ nanoparticles were of low toxicity (**Figure 6.5**). Even at 192 μM, the cell viability was maintained above 80%. On the contrary, incubation with 192 μM $CaWO_4$ nanoparticles reduced the cell viability by over 30% at 24 h.

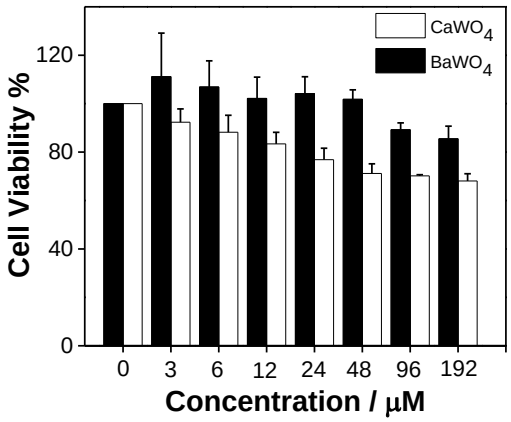

Figure 6.5. Cell viability. 4T1 cells were incubated with PVP-$BaWO_4$ or $CaWO_4$ nanoparticles at various concentrations. Cell viability was measured by MTT assays at 24 h.

We next examined *in vitro* how PVP-$BaWO_4$ or $CaWO_4$ nanoparticles affected intracellular radical levels under irradiation. Briefly, PVP-$BaWO_4$ or $CaWO_4$ nanoparticles (24 μM) were incubated with 4T1 cells for 24 h and then irradiated with 5-Gy X-ray. Intracellular singlet oxygen and hydroxyl radical levels were evaluated at 4 and 24 h. SOSG assays found an increase of intracellular $^1O_2$ level by 17% and 15%, respectively, for PVP-$BaWO_4$ and $CaWO_4$ nanoparticles at 4 h (**Figure 6.6 a, b**). Much greater impact was observed with hydroxyl radical, where APF fluorescence was increased by 9.8- and 6.4-fold, respectively, with PVP-$BaWO_4$ and $CaWO_4$ nanoparticles (**Figure 6.6 c, d**). Interestingly, for $CaWO_4$ nanoparticles, radical elevation was obvious at 4 h but the increase was mitigated over time. For $BaWO_4$ nanoparticles, on the other hand, radical enhancement was significant even at 24 h.

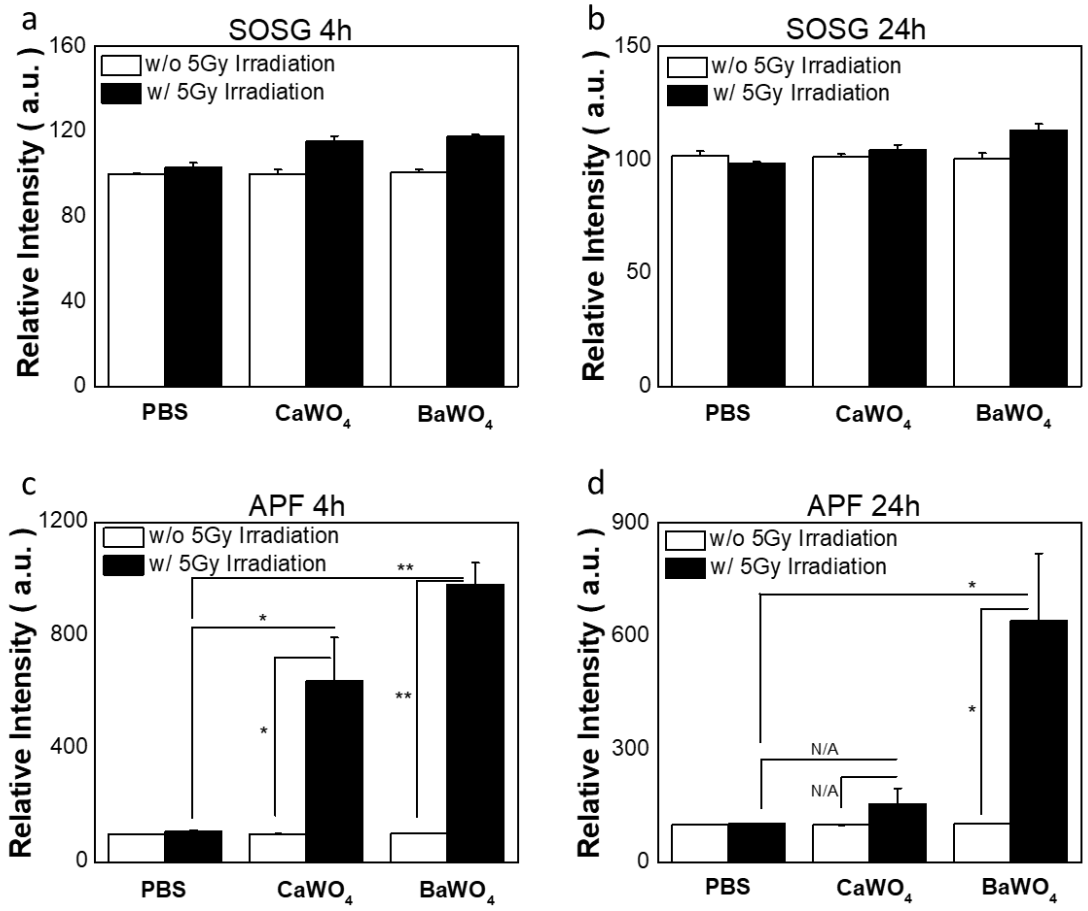

Figure 6.6. Intracellular radical level changes. 4T1 cells were incubated with PVP-$BaWO_4$ or PVP-$CaWO_4$ nanoparticles for either 4 or 24 h, with or without 5 Gy irradiation. (a,b) SOSG to examine intracellular $^1O_2$ levels at (a) 4 h and (b) 24 h. (c,d) APF assays to examine intracellular hydroxyl radical level at (c) 4 h and (d) 24 h. *, P<0.05; **, P<0.01; ***, P<0.001.

The increased radical production translates to elevated cell oxidative stress. Indeed, $BaWO_4$+RT drastically elevated superoxide dismutase (SOD) activity to 1.34 U/mL, compared to 0.71 U/mL for cells receiving RT only (**Figure 6.7 a**). As a comparison, $CaWO_4$+RT only marginally increased SOD activity (0.80 U/mL). Next, MTT assay was performed to assess cell viability change with PVP-$BaWO_4$ and $CaWO_4$ nanoparticles (24 μM) under 5 Gy irradiation (**Figure 6.7 b**). Comparable level of cytotoxicity reduction was observed with these two

nanoparticles (viability 58.5% and 62.5%, respectively, for $CaWO_4$ and $BaWO_4$ nanoparticles). It is worth pointing out, however, that $CaWO_4$ nanoparticles were relatively toxic in the absence of irradiation (**Figure 6.5**).

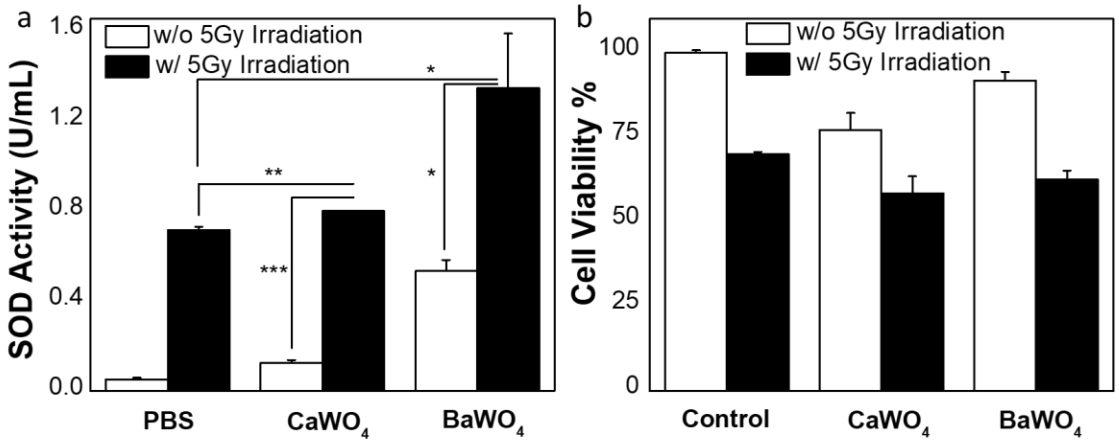

Figure 6.7. (a) SOD activity assays that examine intracellular oxidative stress. 4T1 cells were incubated with PVP-$BaWO_4$ nanoparticles, PVP-$CaWO_4$ nanoparticles, or PBS, and subjected to 5 Gy irradiation. *, $P<0.05$; **, $P<0.01$; ***, $P<0.001$. (b) Cell viability, examined by MTT assays with PVP-$BaWO_4$ or PVP-$CaWO_4$ nanoparticles in the presence or absence of 5 Gy irradiation.

Lastly, we evaluated $BaWO_4$ and $CaWO_4$ nanoparticles *in vivo* in 4T1 bearing mice (n=5). Briefly, 1 million 4T1 cells were inoculated to both flanks of BALB/c mice. When the tumors grew to 100 mm^3, PVP-$BaWO_4$ or $CaWO_4$ nanoparticles were intratumorally injected to the animals (5 mg/mL in 50 μL PBS). For control, 50 μL PBS was injected into animals. Radiation at 10 Gy was delivered to tumors on an X-RAD 320 system 1 h post nanoparticles injection. Tumor dimensions were measured by a caliper everyone 3 days. Significant tumor suppression was observed with $CaWO_4$+RT, leading to a tumor growth inhibition (TGI) rate of 36.9% on Day 18 (**Figure 6.8 a**). Even greater tumor suppression was observed with $BaWO_4$+RT, causing a TGI rate of 69.8% on Day 18 ($P<0.01$). Meanwhile, no sign of acute or long-term toxicity was observed

in animals treated with $BaWO_4$+RT. After 18 days, animals were euthanized and the tumors were harvested. H&E staining results agreed with tumor growth curves, finding reduced cell density in tumors in the $BaWO_4$+RT group (**Figure 6.8 b**).

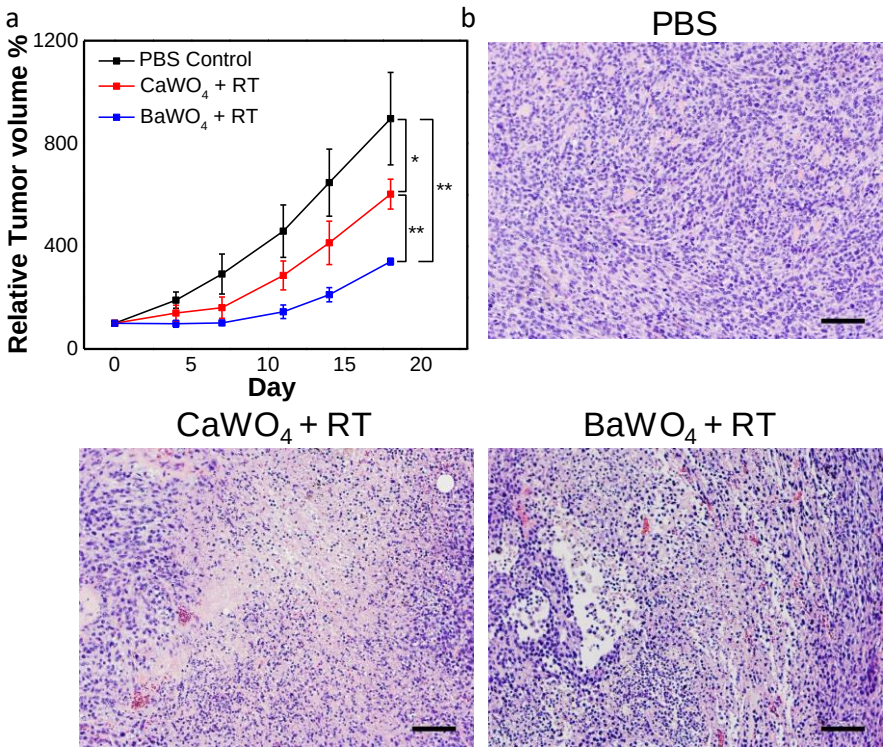

Figure 6.8. (a) Tumor growth curves. 4T1-tumor-bearing animals were intratumorally injected with PVP-$BaWO_4$ nanoparticles, PVP-$CaWO_4$ nanoparticles, or PBS. 10 Gy irradiation was applied to tumors, with the rest of the animal body shielded with lead. *, $P<0.05$; **, $P<0.01$. (b) H&E staining with tumor sections taken from the three treatment groups. Scale bars, 100 μM.

Discussion

We have synthesized PVP-coated $BaWO_4$ nanoparticles and assessed their potential as a novel type of radiosensitizer. For comparison, we have also studied $CaWO_4$ nanoparticles, another type of alkaline earth metal tungstate. Previously, high-Z nanoparticles made of gold, HfO_2, as

well as gadolinium, silver, bismuth, iron oxide, have been tested for their radiosensitizing effects.[11, 16-18, 20, 32-35] To our best knowledge, $BaWO_4$ nanoparticles have never been investigated for RT. When tested in cells, $BaWO_4$ nanoparticles outperformed $CaWO_4$ nanoparticles, manifested in a higher level of cellular oxidative stress they induce under irradiation. More effective tumor suppression was also observed with $BaWO_4$+RT than with $CaWO_4$+RT. Meanwhile, relatively low toxicity was found with PVP-$BaWO_4$ nanoparticles in the absence of radiation. All of these suggest the potential of PVP-$BaWO_4$ nanoparticles as a radiosensitizer.

Bare $BaWO_4$ nanoparticles are poorly dispersed in aqueous solutions. To improve colloidal stability, we have coated the nanoparticles with PVP, which is a safe and water-soluble polymer. It is certainly possible to explore other types of polymer coatings such as polyethylenimine (PEI), polyethylene glycol (PEG) and chitosan, or inorganic coatings such as silica coating. It is also plausible to couple targeting peptides or antibodies onto nanoparticles to improve nanoparticle uptake by cancer cells. These will be investigated in our future studies.

For high-Z radiosensitizers, it is a common approach to inject nanoparticles directly into tumors. For instance, in ongoing clinical trials, HfO_2 nanoparticles are intratumorally injected to enhance RT.[19-22] To this end, we have developed synthesis and surface modification protocols that are straightforward and scalable, and the resulting nanoparticles are amenable to high-dose local injection. It is worthwhile to explore nanoparticles that can be intravenously administered. It is expected that these nanoparticles can accumulated in tumors through the enhanced permeability and retention (EPR) effect or ligand-receptor binding. To this end, however, it might be necessary to assess the size and surface impact on nanoparticle pharmacokinetics.

REFERENCE

CHAPTER 1:

[1] Chen H, Zhang W, Zhu G, et al. *Nat. Rev. Mater.* **2017**;2(7):1-18.

[2] Jiang W, Yin L, Chen H, et al. *Adv Mater* **2019**;31(46):1904058.

[3] Zhou S, Zhen Z, Paschall A V, et al. *Adv. Funct. Mater.* **2021**;31(7):2007017.

[4] Wang R, Cao Z, Wei L, et al. *Nanomed. Nanotechnol. Biol. Med*. **2020**;28:102230.

[5] Yang X, Zhang W, Jiang W, et al. *J. Nanobiotechnol.* **2021**;19(1):1-11.

[6] Cline B L, Jiang W, Lee C, et al. *ACS nano,* **2021**;15(11):17401-17411.

[7] Shumilina E, Huber S M, Lang F. *Am J Physiol Cell Physiol* **2011**;300(6):C1205-C1214.

[8] Binnewies M, Roberts E W, Kersten K, et al. *Nat. Med.* **2018**;24(5):541-550.

[9] Zitvogel L, Tesniere A, Kroemer G. *Nat. Rev. Immunol.* **2006**;6(10):715-727.

[10] Kumar V, Patel S, Tcyganov E, et al. *Trends in Immunology* **2016**;37(3):208-220.

[11] Noy R, Pollard J W. *Immunity* **2014**;41(1):49-61.

[12] Saraiva M, O'garra A. *Nat. Rev. Immunol.* **2010**;10(3):170-181.

[13] Pickup M, Novitskiy S, Moses H L. *Nat. Rev. Cancer* **2013**;13(11):788-799.

[14] Gorelik L, Flavell R A. *Nat. Rev. Immunol.* **2002**;2(1):46-53.

[15] Dunn G P, Old L J, Schreiber R D. *Annu. Rev. Immunol.* **2004**;22:329-360.

[16] Hanahan D, Weinberg R A. *Cell* **2011**;144(5):646-674.

[17] Detappe A, Kunjachan S, Sancey L, Motto-Ros V. *J Control Release* **2016**;238:103-13.

[18] Detappe A, Kunjachan S, Rottmann J. *Cancer Nanotechnol* **2015**;6(1):1-9.

[19] Bonvalot S, Pechoux CL, Baere TD. *J Clin Oncol* **2014**;32(15_suppl):10563.

[20] Liu Y, Zhang P, Li F, Jin X, Li J, Chen W. *Theranostics* **2018**;8(7):1824.

[21] Bonvalot S, Le Pechoux C, De Baere T. *Clin Cancer Res* **2017**;23(4):908- 17.

[22] Bonvalot S, Rutkowski PL, Thariat J. *Lancet Oncol* **2019**;20(8):1148-59.

[23] Seibert JA, Boone JM. *J Nucl Med Technol* **2005**;33(1):3-18.

[24] Zdesenko YG, Avignone Iii FT. *Nucl Instrum Meth A* **2005**;538(1):657-67.

[25] Shmilevich A, Weiss D, Chen R. *Radiat Prot Dosim* **1999**;84(1-4):131-3.

[26] Lee J, Choi S, Kim KH, Heng HG. *Bioconjugate Chem* **2017**;28(1):171-82.

[27] Jo SD, Lee J, Joo MK, Pizzuti VJ. *ACS Biomater Sci Eng* **2018**;4(4):1445-62.

[28] Koczkur KM, Mourdikoudis S, Polavarapu L. *Dalton T* **2015**;44(41):17883-905.

[29] Lee H-Y, Lee S-H, Xu C, Xie J, Lee J-H, Wu B. *Nanotechnology* **2008**;19(16):165101.

[30] Shumilina E, Huber S M, Lang F. *Am J Physiol Cell Physiol* **2011**;300(6):C1205-C1214.

[31] Monteith G R, McAndrew D, Faddy H M, et al. *Nat. Rev. Cancer* **2007**;7(7):519-530.

[32] Berridge M J, Bootman M D, Roderick H L. *Nat. Rev. Mol. Cell Biol.* **2003**;4(7):517-529.

[33] Liu C, Hermann T E. *J. Biol. Chem.* **1978**;253(17):5892-5894.

[34] Feske S. *Nat. Rev. Immunol.* **2007**;7(9):690-702.

[35] Kato M, Neil T K, Fearnley D B, et al. *Int. Immunol.* **2000**;12(11):1511-1519.

CHAPTER 3:

[1] Tel J, Benitez-Ribas D, Hoosemans S, et al. *Eur J Immunol.* **2011**;41(4):1014-1023.

[2] Mahnke K, Guo M, Lee S, et al. *J Cell Biol.* **2000**;151(3):673-683.

[3] Schreibelt G, Klinkenberg L J J, Cruz L J, et al. *Blood* **2012**;119(10):2284-2292.

[4] Jiang W, Yin L, Chen H, et al. *Adv Mater* **2019**;31(46):1904058.

CHAPTER 6:

[1] Ko EC, Raben D, Formenti SC. *Clin Cancer Res* **2018**;24(23):5792.

[2] Baker S, Dahele M, Lagerwaard FJ, Senan S. *Radiat Oncol* **2016**;11(1):115.

[3] Hickey BE, James ML, Lehman M, Hider PN. *Cochrane DB Syst Rev* **2016**(7).

[4] Lukas RV, Wainwright DA, Ladomersky E, Sachdev S. *Brain* **2019**;33(3).

[5] Zhang Y, Chen Z, Li J. *Medicine* **2017**;96(40).

[6] Stone HB, Coleman CN, Anscher MS, McBride WH. *Lancet Oncol* **2003**;4(9):529-36.

[7] Gao S, Zhang W, Wang R, Hopkins SP. *ACS Nano* **2020**;14(2):1468-81.

[8] Liu J, Zhang W, Kumar A, Rong X, Yang W. *Bioconjugate Chem* **2020**;31(1):82-92.

[9] Wang H, Mu X, He H, Zhang XD. *Trends Pharmacol Sci* **2018**;39(1):24-48.

[10] Wardman P. *Clin Oncol* **2007**;19(6):397-417.

[11] Song G, Cheng L, Chao Y, Yang K, Liu Z. *Adv Mater* **2017**;29(32).

[12] Hainfeld JF, Slatkin DN, Smilowitz HM. *Phys Med Biol* **2004**;49(18):N309-N15.

[13] Chattopadhyay N, Cai Z, Pignol J-P, Keller B. *Mol Pharm* **2010**;7(6):2194-206.

[14] Chithrani DB, Jelveh S, Jalali F, Prooijen Mv. *Radiat Res* **2010**;173(6):719-28.

[15] Haume K, Rosa S, Grellet S, Śmiałek MA. *Cancer Nanotechnol* **2016**;7(1):8.

[16] Lux F, Sancey L, Bianchi A, Crémillieux Y. *Nanomedicine* **2015**;10(11):1801-15.

[17] Detappe A, Kunjachan S, Sancey L, Motto-Ros V. *J Control Release* **2016**;238:103-13.

[18] Detappe A, Kunjachan S, Rottmann J. *Cancer Nanotechnol* **2015**;6(1):1-9.

[19] Bonvalot S, Pechoux CL, Baere TD. *J Clin Oncol* **2014**;32(15_suppl):10563.

[20] Liu Y, Zhang P, Li F, Jin X, Li J, Chen W. *Theranostics* **2018**;8(7):1824.

[21] Bonvalot S, Le Pechoux C, De Baere T. *Clin Cancer Res* **2017**;23(4):908-17.

[22] Bonvalot S, Rutkowski PL, Thariat J. *Lancet Oncol* **2019**;20(8):1148-59.

[23] Seibert JA, Boone JM. *J Nucl Med Technol* **2005**;33(1):3-18.

[24] Zdesenko YG, Avignone Iii FT. *Nucl Instrum Meth A* **2005**;538(1):657-67.

[25] Shmilevich A, Weiss D, Chen R. *Radiat Prot Dosim* **1999**;84(1-4):131-3.

[26] Lee J, Choi S, Kim KH, Heng HG. *Bioconjugate Chem* **2017**;28(1):171-82.

[27] Jo SD, Lee J, Joo MK, Pizzuti VJ. *ACS Biomater Sci Eng* **2018**;4(4):1445-62.

[28] Koczkur KM, Mourdikoudis S, Polavarapu L. *Dalton T* **2015**;44(41):17883-905.

[29] Lee H-Y, Lee S-H, Xu C, Xie J, Lee J-H, Wu B. *Nanotechnology* **2008**;19(16):165101.

[30] Kim DH, Wei A, Won Y-Y. *ACS Appl Mater Inter* **2012**;4(4):1872-7.

[31] Rota C, Chignell CF, Mason RP. *Free Radical Bio Med* **1999**;27(7):873-81.

[32] Seo S-J, Han S-M, Cho J-H, Hyodo K. *Radiat Environ Bioph* **2015**;54(4):423-31.

[33] Zhang H, Patel N, Ding S, Xiong J, Wu P. *Biomater Sci* **2016**;4(2):288-98.

[34] Song G, Liang C, Gong H, Li M, Zheng X, Cheng L. *Adv Mater* **2015**;27(40):6110-7.

[35] Wang S, Li X, Chen Y, Cai X, Yao H, Gao W. *Adv Mater* **2015**;27(17):2775-82.

APPENDICES

A Supporting information for Chapter 2

Characterizations of nanoparticles. Scanning Electron Microscopy (SEM) and Energy Dispersive X-ray Spectra (EDS) elemental mapping images were acquired on a FEI Teneo field emission SEM equipped with an Oxford EDS system. Transmission Electron Microscopy (TEM) was carried out on an FEI Tecnai20 transmission electron microscope operating at an accelerating voltage of 200 kV. High resolution TEM analysis was performed on a Hitachi transmission electron microscope H9500 operating at a 300 kV accelerating voltage. X-ray diffraction (XRD) analysis was carried out on a Bruker D8- Advance using dried samples placed on a cut glass slide with Cu Kα1 radiation (λ = 1.5406 Å). Particle size by Dynamic Light Scattering (DLS) and zeta potential measurements were carried out on a Malvern Zetasizer Nano ZS system. Fourier-transform infrared (FT-IR) spectra were recorded on a Nicolet iS10 FT-IR spectrometer.

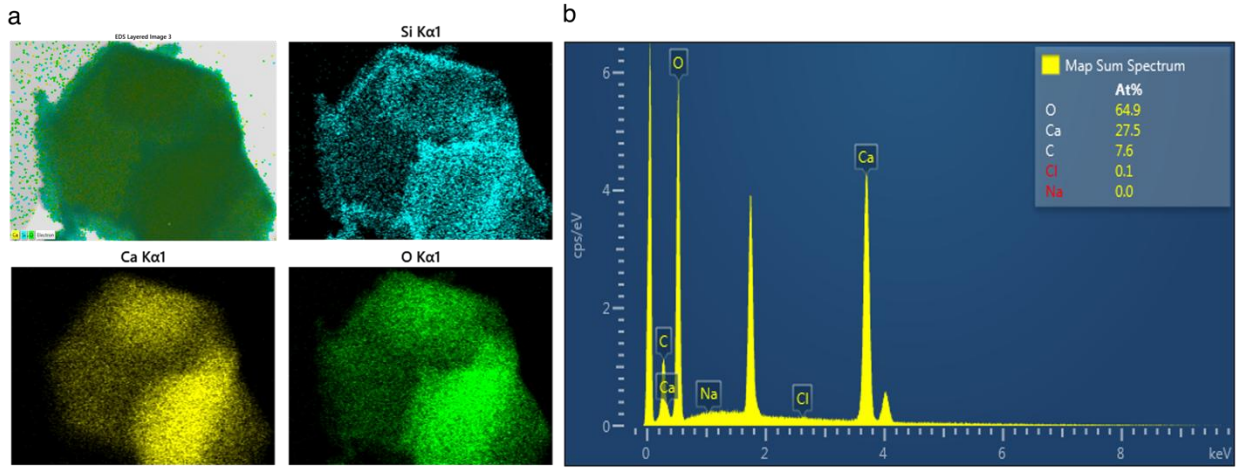

Figure S2.1. a) EDS elemental mapping of Ca, O and Si in SCHNPs. **b)** EDS elemental mapping spectrum in CHNPs.

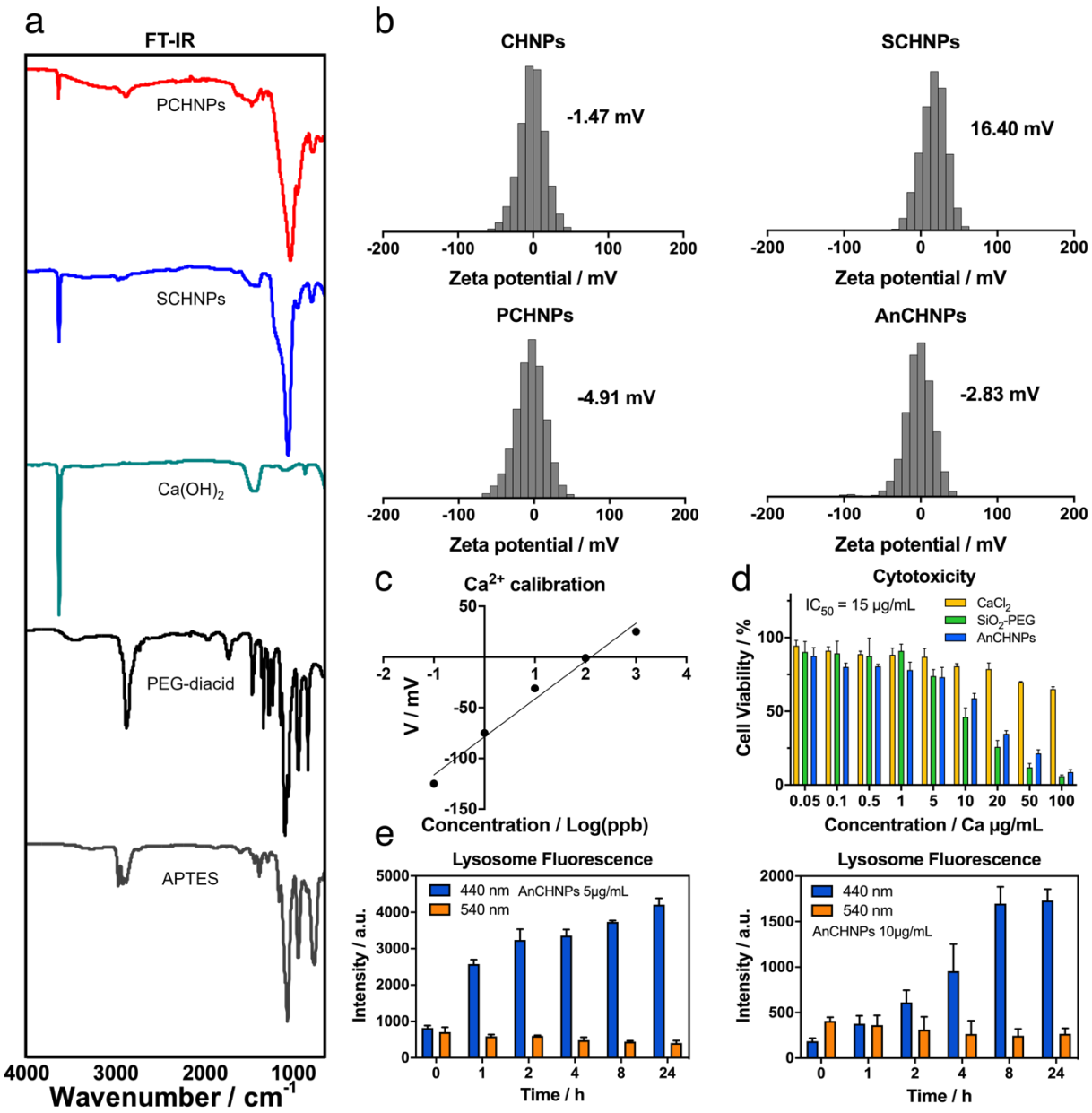

Figure S2.2. Characterizations of $Ca(OH)_2$ nanoparticles. **a)** FT-IR spectra of CHNPs, SCHNPs, PCHNPs and references. **b)** Zeta-potential distribution of CHNPs, SCHNPs, PCHNPs and AnCHNPs. **c)** Calibration of Ca^{2+} concentration. **d)** Concentration-dependent cytotoxicity of AnCHNPs to DC. **e)** lysosomal pH change revealed by lysosome fluorescence.

B Supporting information for Chapter 3

Stability and release experiments. CHNPs and PCHNPs were dispersed in 100 µl ammonium acetate buffers (pH=5.5 or pH=7.4) and added into a Slide-A-LyzerTM MINI Dialysis Device (MWCO = 2K, Cat # 69550, ThermoFisher, US). The unite was placed into a 5 mL Eppendorf tube containing 4.5 mL ammonium acetate buffer (pH=5.5 or pH=7.4). The tube was kept on the shaker (20 rpm) at room temperature. At different time points (0, 15 mins, 0.5, 1, 2, 4, 8, 10, 24 h), 500 µL of PCHNPs solution was taken from the Eppendorf tube to test the free Ca^{2+} ions concentration, followed by addition of another 500 µL fresh buffer to keep total volume at 4.5 mL in tube. A Ca^{2+} electrode (HORIBA LAQUAtwin Ca-11) was used to measure free Ca^{2+} ions. All measurements were performed following the manufacture's protocol and repeated in triplicate. TEM photos were taken as the same technique in characterizations at different time points 0, 2, 4, 8, 12, 24 h of PCHNPs dispersed in Milli Q H_2O to check the morphology of PCHNPs degradation.

Cell culture. B16F10-OVA cells (murine melanoma) were grown in high glucose DMEM (ATCC® 30-2002TM) with addition of G418 ingredient. B16F10 cells (murine melanoma) were grown in high glucose DMEM (ATCC® 30-2002TM). MB49 cells (murine bladder carcinoma) were grown in RPMI-1640 (Corning, 10-040-CV). Bone marrow derived dendritic cells (BMDCs) were established from germ cells extracted from bone marrow of C57BL/6 mice and cultured in RPMI-1640 (Corning, 10-040-CV) with addition of GM-SCF according to an existing protocol.[4] All cell culture mediums were supplemented with 10% fetal bovine serum (FBS) and 100 units/mL

of penicillin and 100 units/mL streptomycin (MediaTech, USA). All cells were maintained in a humidified, 5% carbon dioxide atmosphere at 37 °C.

Cell cytotoxicity. ATPlite-1step luminescence assay kit (PerkinElmer, Lot # 107-21051) was used to determine cellular ATP contents following the manufacturer's protocol. BMDCs were seeded into 96-well plates at the density of 1×10^4 cells per well and incubated overnight. Then the cells were treated with $CaCl_2$ solution, SiO_2-PEG or AnCHNPs at a dose range of 0.05-100 μg Ca/mL (SiO_2-PEG dose range 0.05-100 μg/mL) for 24 h. The luminescence intensity of each well was measured on a microplate reader (Synergy Mx, BioTeK) and normalized to that of control cells.

Lysosome pH change. LysoSensor™ Yellow/Blue DND-160 (PDMPO) kit (Invitrogen, Lot # 2174576) was used to study lysosomal pH change from internalization of AnCHNPs by BMDCs, following the manufacturer's protocol. Briefly, BMDCs were seeded into 96-well plates at the density of 1×10^4 cells per well and incubated overnight. At different time points (0, 1, 2, 4, 8, 24 h), medium from certain wells was removed and prewarmed (37°C) probe-containing (1 μM) medium was added. Cells were incubated for 5 mins under the same growth conditions. Then the loading solution was replaced with fresh medium and the fluorescences (dual-excitation at 329, 384 nm and dual-emission at 440, 540 nm) were observed using a microplate reader (Synergy Mx, BioTeK). In acidic organelles LysoSensor™ Yellow/Blue DND-160 (PDMPO) has predominantly yellow fluorescence, and in less acidic organelles it has blue fluorescence. Dual-emission measurements indicate the change of the pH in lysosome via the ratio of blue/yellow fluorescence.

Intracellular Ca^{2+} concentration ($[Ca^{2+}]$). Fluo-3 AM kit (Cayman, 14960) was used to measure the intracellular $[Ca^{2+}]$ change from internalization of AnCHNPs by BMDCs, following the manufacturer's protocol. Briefly, BMDCs were seeded into 96-well plates at the density of 1×10^4 cells per well and incubated overnight. At different time points (0, 1, 2, 4, 8, 24 h), the medium from certain wells was removed and prewarmed (37°C) probe-containing (5 μM) medium was added. Cells were incubated for 30 mins under the same growth conditions. Then the loading solution was replaced with fresh medium to remove any dye that was nonspecifically associated with the cell surface, and cells were incubated for a further 30 mins to allow complete de-esterification of intracellular acetoxymethyl esters. Fluorescence was observed (excitation at 485 nm, emission at 520 nm) using a microplate reader (Synergy Mx, BioTeK).

***In vitro* flow cytometry study of maturation, migration, activation and antigen-presentation of BMDCs.**

1. **Maturation.** BMDCs at a density of 1×10^6 cells per well were seeded in a 6-well plate one day before the experiment. Certain cells were set under different treatment conditions: None as blank control, $CaCl_2$ solution 5 μg/mL and 10 μg/mL, AnCHNPs 5 μg/mL and 10 μg/mL. After 24 h incubation, supernatants were removed and BMDCs were harvested by cell lifter to be prepared for flow cytometry measurements. MHCII-FITC (#107616) and CD205-APC (#138206) were used to check the mature BMDCs population in each group.
2. **Migration.** B16F10-OVA cancer cells were treated with 100 Gy X-ray irradiation and transferred into lower chambers of 6-well Transwell® Permeable Supports system at a density of 1×10^5 cells per well (one well of B16F10-OVA cancer cells with no irradiation as blank control). CFSE-labeled BMDCs at a density of 1×10^6 cells per well were seeded in the upper

chamber of the wells under different treatment conditions: None, $CaCl_2$ solution 5 μg/mL and 10 μg/mL, AnCHNPs 5 μg/mL and 10 μg/mL. After 24 h incubation, all cells in the lower chambers were harvested by cell lifter to be prepared for flow cytometry measurements to analyze the percentage of CFSE-BMDCs in cells of each well.

3. **Activation and Antigen-presentation.** B16F10-OVA cancer cells were treated with 100 Gy X-ray irradiation and transferred into wells of 6-well plate at a density of 1×10^5 cells per well (one well of B16F10-OVA cancer cells with no irradiation as blank control). BMDCs at a density of 1×10^6 cells per well were seeded in each well under different treatment conditions: None, $CaCl_2$ solution 5 μg/mL and 10 μg/mL, AnCHNPs 5 μg/mL and 10 μg/mL. After 24 h incubation, all cells in each well were harvested by cell lifter to be prepared for flow cytometry measurements to analyze certain population of BMDCs in each well. MHCII-FITC (#107616), CD80-PerCP-Cy5.5 (#560526) and CD86-BV605 (#563055) were used to check the activation of BMDCs population. CD40-PE (#12-0401-83) and OVA-APC (#17-5743-82) were used to check the antigen-presentation of BMDCs population.

In vitro **cytokine secretion.** BMDCs at a density of 1×10^5 cells per well were seeded in a 48-well plate one day before the experiment. B16F10-OVA cancer cells were treated with 100 Gy X-ray irradiation and transferred into previous wells at a density of 1×10^4 cells per well (one well with no cancer cells as blank control). Then certain wells were set under different treatment conditions: None, $CaCl_2$ solution 5 μg/mL and 10 μg/mL, AnCHNPs 5 μg/mL and 10 μg/mL. After 24 h incubation, the supernatants were collected and IL-6, IL-10, IL-12, TNF-α contents were quantified using R&D Systems Mouse IL-6, IL-10, IL-12, TNF-α DuoSet ELISA (Minneapolis,

MN) following the manufacturer's protocol. Results were analyzed with Four Parameter Logistic Curve method from Myassay.com.

Western blot analysis. BMDCs were seeded into 100 mm petri dish at the density of 5×10^5 cells and incubated overnight. Then the cells were treated with OVA (10 μg/mL) in PBS as control and OVA (10 μg/mL) + AnCHNPs (5 μg/mL) in PBS. After 24 h of incubation, cell lysates were prepared by homogenizing cells in a RIPA buffer supplemented with 1× proteinase inhibitor cocktail (Amresco). Protein concentration was determined using a bicinchoninic acid (BCA) protein assay kit (Thermo Fisher Scientific). Protein lysates were loaded onto 10% SDS-PAGE and were transferred to PVDF membrane. Nonspecific binding to the membrane was blocked by incubation with 5% nonfat milk at room temperature for 1 h. The membranes were incubated for 16 hours at 4 °C with primary antibodies at the dilutions specified by the manufacturers. After secondary antibody incubation for 1 h at room temperature, membranes were treated with ECL reagents (Thermo Fisher Scientific) and exposed to X-ray films (Santa Cruz). All the imaging results were analyzed by ImageJ.

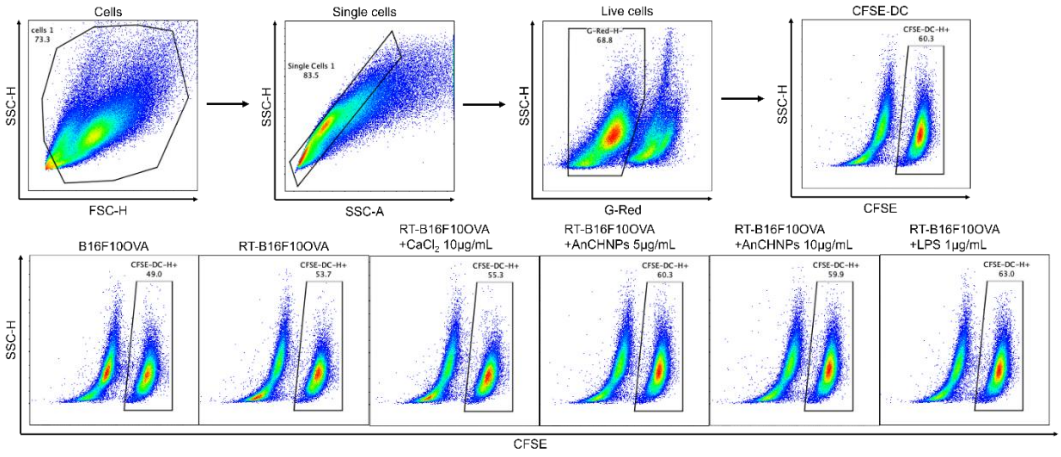

Figure S3. Flow cytometry gating strategy for DC migration

C Supporting information for Chapter 4

Animal model. All experimental procedures were conducted following a protocol approved by the Institutional Animal Care and Use Committee (IACUC) of the University of Georgia. C57BL/6 mice (4 weeks old female) were purchased from Envigo laboratories and maintained under pathogen-free conditions. The animal model was established by subcutaneously injecting 2×10^5 B16F10-OVA / B16F10 / MB49 cells in 50 μL PBS into the right hind limb of each mouse after 2 weeks of settlement (6 weeks old).

***In vivo* flow cytometry study of immune response profiling.** C57BL/6 mice bearing B16F10-OVA tumors were randomly divided into three groups (n=10 for each group): (1) 10 Gy X-ray irradiation + PBS; (2) 10 Gy X-ray irradiation + $CaCl_2$ solution (0.2 mg Ca/kg); (3) 10 Gy X-ray irradiation + AnCHNPs (0.2 mg Ca/kg). After tumor size reached 100-150 mm^3 on average, treatments were intratumorally injected on day 0. All injections were performed at five sites of the tumor to ensure good coverage. $CaCl_2$ and AnCHNPs were injected in 50 μL PBS, 1 h after the X-ray irradiation was performed on mice. On day 3 and day 7 respectively, 5 mice of each group were euthanized and tumor, spleen, lymph nodes were harvested for immune response profiling. The tumor pieces obtained for single-cell analysis were cut into smaller pieces with scissors and digested in DMEM with 1 mg/mL collagenase type V (Worthington Biochemical Corporation) at 37 °C for 45 mins. The digested tissues were gently meshed though a 250 μm cell strainer (Thermo scientific, Lot # UB2685874A). Red blood cells were lysed by Ack lysing buffer (Gibco) according to the manufacturer's instructions. The single-cell suspensions were washed with cold sterile PBS and resuspended in staining buffer. Following cell counting and aliquoting, staining

was performed by using various combinations of fluorophore-conjugated antibodies for 30 mins at 4 °C. Spleen and lymph nodes were processed by similar procedures, with 70 μm cell strainer (Corning Falcon, Ref # 352235) to obtain single cell suspension in staining buffer expect for no need of digestion process with collagenase type V. The following anti-mouse antibodies were purchased from BD Biosciences: CD45-APC-Cy7 (#557659), CD4-BV605 (#563151), FoxP3-PE (#563101), CD11c-PE-Cy7 (#558079), CD86-BV605 (#563055), CD80-PerCP-Cy5.5 (#560526). CD40-PE (#12-0401-83) was purchased from Invitrogen. OVA-APC (#17-5743-82) was purchased from eBioscience. MHCII-FITC (#107616), CD205-APC (#138206), IFN-γ-APC (#505810), CD3-FITC (#100206) and CD8-BV510 (#100752) were purchased from BioLegend. Live/dead DAPI was purchased from Thermal Fisher. Multi-parameter staining was used to identify the following populations of interest: (a) $CD8^+$ T cells ($CD45^+CD3^+CD8^+$), (b) $CD8^+IFN\gamma^+$ T cells ($CD45^+CD3^+CD8^+IFN\gamma^+$), (c) $CD4^+$ T cells ($CD45^+CD3^+CD4^+$), (d) Treg cells ($CD45^+CD3^+CD4^+FoxP3^+$), (e) $MHCII^+$ DCs ($CD11c^+MHCII^+$), (f) $CD80^+$ DCs ($CD11c^+MHCII^+CD80^+$), (g) $CD86^+$ DCs ($CD11c^+MHCII^+CD86^+$), (h) $CD40^+$ DCs ($CD11c^+MHCII^+CD40^+$), (i) OVA^+ DCs ($CD11c^+MHCII^+$ SIINFEKL-H-$2Kb^+$). For intracellular FoxP3 and IFN-γ staining, cells were further fixed and permeabilized using Permeabilization Solution Kit (BD, 554714). After washing, cells were used for flow cytometry analysis (Quanteon, Agilent). For tumor-specific T-cell response, splenocytes were co-cultured w/ or w/o B16F10-OVA cells for another 6 h before staining for flow cytometry analysis. The data were processed by FlowJo 10.0. Doublets were excluded based on forward and side scatter. Dead cells were excluded based on positive signal of DAPI staining.

***In vivo* cytokine secretion.** Blood samples were collected from the same batch of mice undergo *in vivo* flow cytometry study and blood serum were obtained after centrifugation on both day 3 and day 7. IL-1β, IL-6, IL-10, IL-12, TNF-α, IFN-γ contents in these serum samples were quantified using R&D Systems Mouse IL-1β, IL-6, IL-10, IL-12, TNF-α, IFN-γ DuoSet ELISA (Minneapolis, MN) following the manufacturer's protocol. Results were analyzed with Four Parameter Logistic Curve method from Myassay.com.

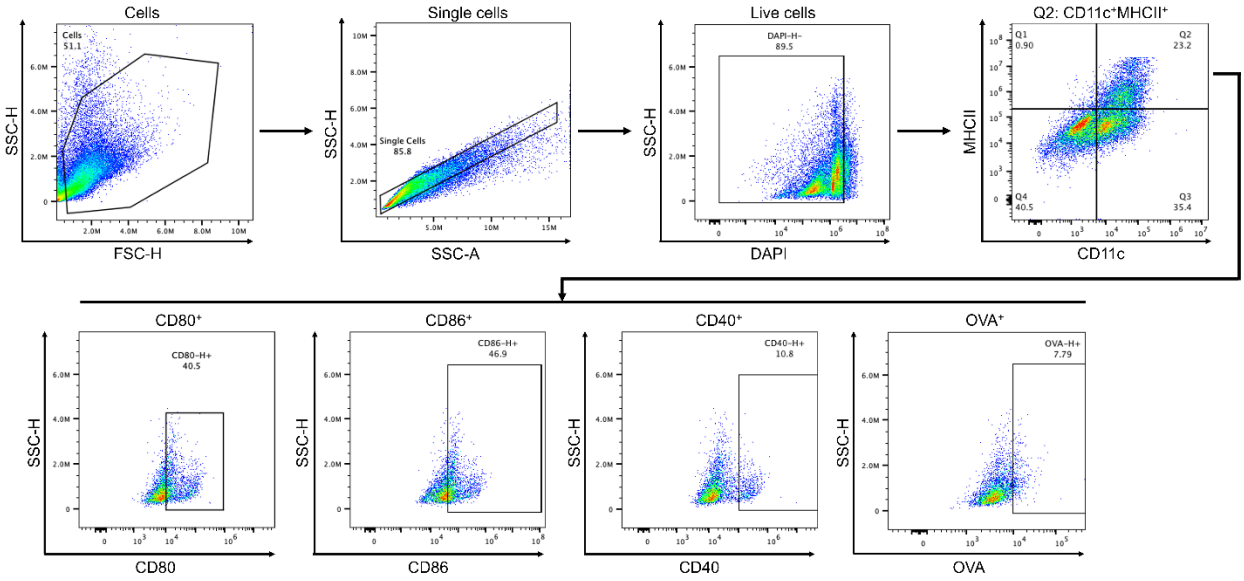

Figure S4.1. Flow cytometry gating strategy of dendritic cell biomarkers.

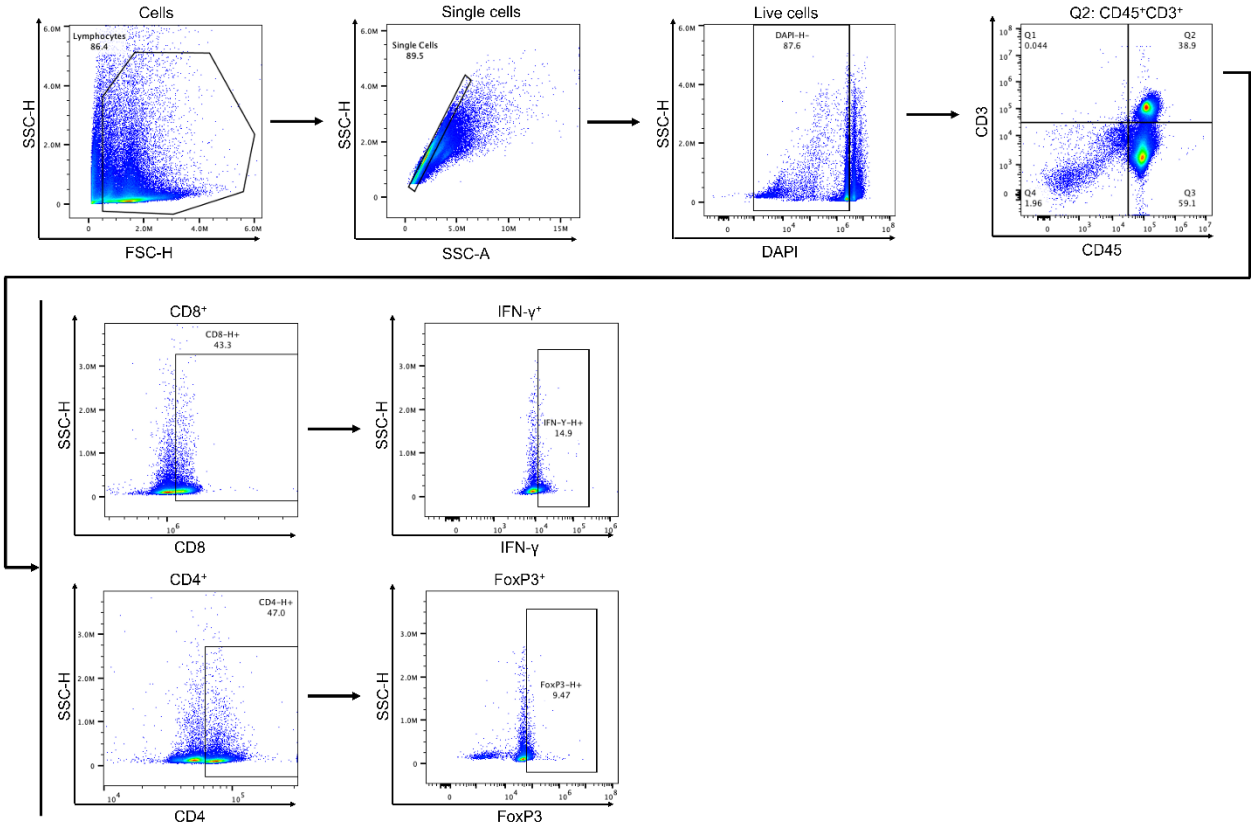

Figure S4.2. Flow cytometry gating strategy for T cell biomarkers.

D Supporting information for Chapter 5

Therapy study.

Combination with radiotherapy: C57BL/6 mice bearing B16F10-OVA tumors were randomly divided into 6 groups (n=5 for each group): (1) PBS, no irradiation; (2) 0.2 mg Ca/kg AnCHNPs (AnCHNPs); (3) 10 Gy X-ray irradiation + PBS (RT+PBS); (4) 10 Gy X-ray irradiation + 0.2 mg Ca/kg AnCHNPs (RT+AnCHNPs); (5) 10 Gy X-ray irradiation + 0.2 mg Ca/kg AnCHNPs + 10 mg/kg Anti-CD8 (RT+AnCHNPs+αCD8); (6) 10 Gy X-ray irradiation + 0.2 mg Ca/kg AnCHNPs + 10 mg/kg Anti-CD4 (RT+AnCHNPs+αCD4). After tumor size reached 35-50 mm^3 on average, anti-PD-1 were intraperitoneally injected and AnCHNPs were intratumorally injected on day 0 and day 2. Anti-CD8 and anti-CD4 were intraperitoneally injected on day 0 and day 4. All injections were performed at five sites of the tumor to ensure good coverage. Antibodies and AnCHNPs were injected in 100 μL and 50 μL PBS respectively, 1 h after the X-ray irradiation was performed on mice. The tumor size and body weight were inspected every day. The tumor was measured in two dimensions with a caliper and tumor volume was estimated as $(\text{length})\times(\text{width})^2/2$. After therapy, major organs as well as tumors were collected and sectioned into 4-μm slices for H&E and Ki-67 staining.

Combination with chemotherapy: C57BL/6 mice bearing B16F10-OVA tumors were randomly divided into 3 groups (n=5 for each group): (1) PBS; (2) 40 mg/kg Carboplatin (Carboplatin); (3) 40 mg/kg Carboplatin + 0.2 mg Ca/kg AnCHNPs (Carboplatin+AnCHNPs). After tumor size reached 35-50 mm^3 on average, carboplatin was intraperitoneally injected on day 0 and AnCHNPs

were intratumorally injected on day 0 and day 2. All injections were performed at five sites of the tumor to ensure good coverage. Carboplatin and AnCHNPs were injected in 100 μL and 50 μL PBS respectively. The tumor size and body weight were inspected every day. The tumor was measured in two dimensions with a caliper and tumor volume was estimated as $(\text{length})\times(\text{width})^2/2$.

Combination with immunotherapy: C57BL/6 mice bearing B16F10-OVA tumors were randomly divided into 5 groups (n=5 for each group): (1) PBS; (2) 10 mg/kg Anti-PD-1 (αPD-1); (3) 10 mg/kg Anti-PD-1 + 0.2 mg Ca/kg AnCHNPs (αPD-1+AnCHNPs); (4) 10 Gy RT + 10 mg/kg Anti-PD-1 (RT+αPD-1); (5) 10 Gy RT + 10 mg/kg Anti-PD-1 + 0.2 mg Ca/kg AnCHNPs (RT+αPD-1+AnCHNPs). After tumor size reached 35-50 mm^3 on average, antibodies were intraperitoneally injected and AnCHNPs were intratumorally injected on day 0 and day 2. RT was applied to tumor 1 h prior to injections with rest of body lead-protected. All injections were performed at five sites of the tumor to ensure good coverage. Antibodies and AnCHNPs were injected in 100 μL and 50 μL PBS respectively. The tumor size and body weight were inspected every day. The tumor was measured in two dimensions with a caliper and tumor volume was estimated as $(\text{length})\times(\text{width})^2/2$.

B16F10 tumor model: C57BL/6 mice bearing B16F10 tumors were randomly divided into 3 groups (n=5 for each group): (1) PBS; (2) 10 mg/kg Anti-PD-1 (αPD-1); (3) 10 mg/kg Anti-PD-1 + 0.2 mg Ca/kg AnCHNPs (αPD-1+AnCHNPs). After tumor size reached 35-50 mm^3 on average, antibodies were intraperitoneally injected and AnCHNPs were intratumorally injected on day 0 and day 2. All injections were performed at five sites of the tumor to ensure good coverage. Anti-

PD-1 and AnCHNPs were injected in 100 μL and 50 μL PBS respectively. The tumor size and body weight were inspected every other day. The tumor was measured in two dimensions with a caliper and tumor volume was estimated as (length)×(width)^2/2.

MB49 tumor model: C57BL/6 mice bearing MB49 tumors were randomly divided into 3 groups (n=5 for each group): (1) PBS, no irradiation; (2) 10 Gy X-ray irradiation + PBS (RT+PBS); (3) 10 Gy X-ray irradiation + 0.2 mg Ca/kg AnCHNPs (RT+AnCHNPs). After tumor size reached 35-50 mm^3 on average, treatments were intratumorally injected on day 0 and day 2. All injections were performed at five sites of the tumor to ensure good coverage. AnCHNPs were injected in 50 μL PBS, 1 h after the X-ray irradiation was performed on mice. The tumor size and body weight were inspected every day. The tumor was measured in two dimensions with a caliper and tumor volume was estimated as (length)×(width)^2/2.

Statistical analysis. For *in vitro* study, all measurements were performed in triplicate unless specified otherwise. Data obtained from high-content BioApplication Studio 2.0 were exported and further analyzed using a JMP statistical analysis package (SAS Institute, North Carolina). For *in vivo* study, all measurements were performed three times unless specified otherwise. Half-maximum inhibitory concentration (IC_{50}) was determined by Doseresp using Origin 9. All data were represented as mean ± S.D. Comparisons of multiple assays were performed using one-way ANOVA test and comparisons of two groups were performed using a paired t-test, with P values of 0.05 or less representing statistical significance.

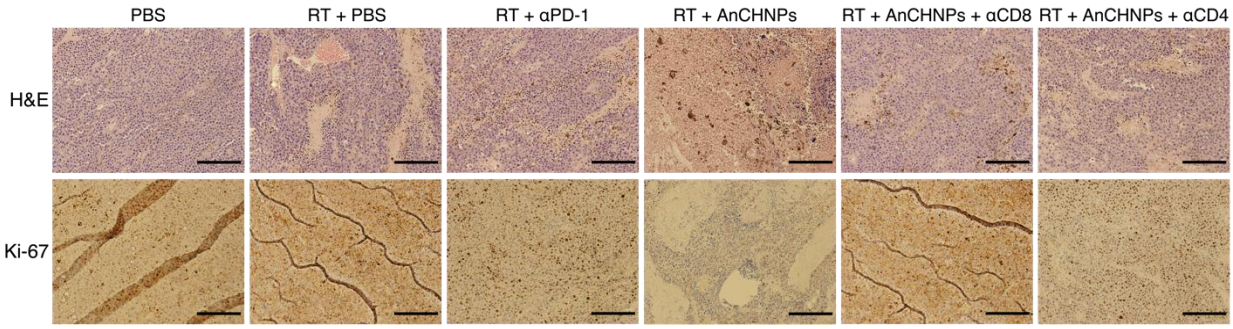

Figure S5.1. H&E and Ki-67 staining images of B16F10-OVA tumors. Scale bar: 200 μm.

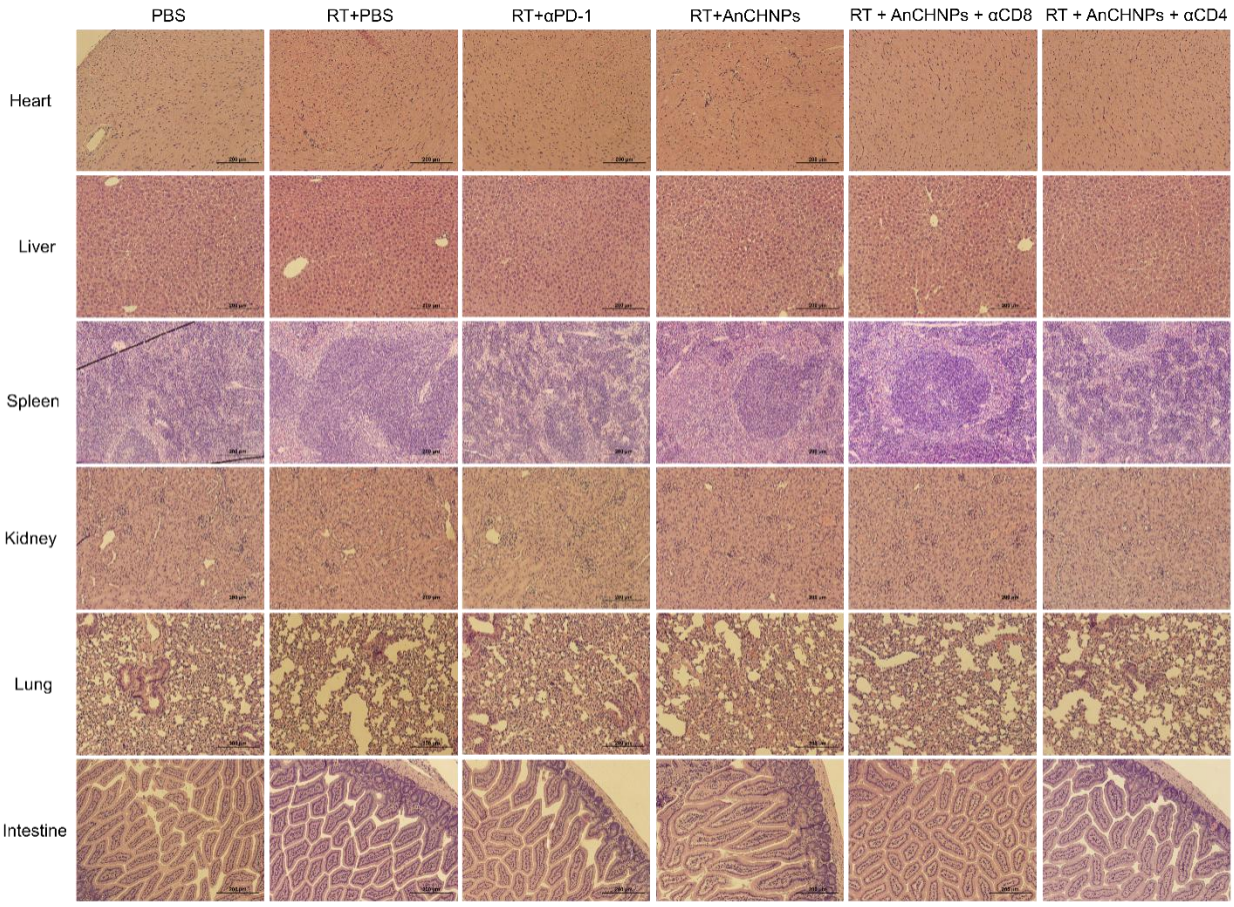

Figure S5.2. H&E staining images of major organs. Scale bar: 200 μm.